Journal of Sedimentary Research

Journal of Sedimentary Research, 2022, v. 92, 896–919
Research Article
DOI: 10.2110/jsr.2022.004

THE GLASS RAMP OF WRANGELLIA: LATE TRIASSIC TO EARLY JURASSIC OUTER RAMP ENVIRONMENTS OF THE MCCARTHY FORMATION, ALASKA, U.S.A.

YORICK P. VEENMA,*[1] KAYLA McCABE,[2] ANDREW H. CARUTHERS,[3] MARTIN ABERHAN,[4] MARTYN GOLDING,[5] SELVA M. MARROQUÍN,[†2] JEREMY D. OWENS,[6] THEODORE R. THEM, II,[7] BENJAMIN C. GILL,[2] AND JOÃO P. TRABUCHO ALEXANDRE[1]

[1]*Department of Earth Sciences, Universiteit Utrecht, Utrecht, the Netherlands*
[2]*Department of Geosciences, Virginia Tech, Blacksburg, Virginia, U.S.A.*
[3]*Department of Geological and Environmental Sciences, Western Michigan University, Kalamazoo, Michigan, U.S.A.*
[4]*Museum für Naturkunde Berlin, Leibniz Institute for Evolution and Biodiversity Science, Berlin, Germany*
[5]*Geological Survey of Canada, Pacific Division, Vancouver, British Columbia, Canada*
[6]*Department of Earth, Ocean and Atmospheric Science, National High Magnetic Field Laboratory, Florida State University, Tallahassee, Florida, U.S.A.*
[7]*Department of Geology and Environmental Geosciences, College of Charleston, Charleston, South Carolina, U.S.A.*
e-mail: j.trabucho@uu.nl

ABSTRACT: **The marine record of the Triassic–Jurassic boundary interval has been studied extensively in shallow-marine successions deposited along the margins of Pangea, particularly its Tethyan margins. Several of these successions show a facies change from carbonate-rich to carbonate-poor strata attributed to the consequences of igneous activity in the Central Atlantic Magmatic Province (CAMP), which included a biocalcification crisis and the end-Triassic mass extinction. Evidence for a decline in calcareous and an increase in biosiliceous sedimentation across the Triassic–Jurassic boundary interval is currently limited to the continental margins of Pangea with no data from the open Panthalassan Ocean, the largest ocean basin. Here, we present a facies analysis of the McCarthy Formation (Grotto Creek, southcentral Alaska), which represents Norian to Hettangian deepwater sedimentation on Wrangellia, then an isolated oceanic plateau in the tropical eastern Panthalassan Ocean.**

The facies associations defined in this study represent changes in the composition and rate of biogenic sediment shedding from shallow water to the outer ramp. The uppermost Norian to lowermost Hettangian represent an ~ 8.9-Myr-long interval of sediment starvation dominated by pelagic sedimentation. Sedimentation rates during the Rhaetian were anomalously low compared to sedimentation rates in a similar lowermost Hettangian facies. Thus, we infer the likelihood of several short hiatuses in the Rhaetian, a result of reduced input of biogenic sediment. In the Hettangian, the boundary between the lower and upper members of the McCarthy Formation represents a change in the composition of shallow-water skeletal grains shed to the outer ramp from calcareous to biosiliceous. This change also coincides with an order-of-magnitude increase in sedimentation rates and represents the transition from a siliceous carbonate-ramp to a glass ramp ~ 400 kyr after the Triassic–Jurassic boundary. Sets of large-scale low-angle cross-stratification in the Hettangian are interpreted as a bottom current–induced sediment drift (contouritic sedimentation). The biosiliceous composition of densites (turbidites) and contourites in the Hettangian upper member reflects the Early Jurassic dominance of siliceous sponges over Late Triassic shallow-water carbonate environments. This dominance was brought about by the end-Triassic mass extinction and the collapse of the carbonate factory, as well as increased silica flux to the ocean as a response to the weathering of CAMP basalts. The presence of a glass ramp on Wrangellia supports the hypothesis that global increases in oceanic silica concentrations promoted widespread biosiliceous sedimentation on ramps across the Triassic to Jurassic transition.

INTRODUCTION

The Triassic–Jurassic boundary interval has been studied extensively in records of neritic sediments deposited along the Tethyan margins of Pangea (Korte et al. 2018, and references therein). Several of these successions document a facies change from carbonate-rich to carbonate-poor strata (see Fig. 5 in Greene et al. 2012; Ritterbush et al. 2014), which has been attributed to ocean acidification and a biocalcification crisis. This facies change is accompanied by a negative excursion in the carbon isotope record that has been linked to outgassing of CO_2 and CH_4 from the Central Atlantic Magmatic Province (CAMP) (e.g., Galli et al. 2005; Črne et al. 2011).

Along the margins of Pangea (Fig. 1), a transition from carbonate to "glass" ramps has been recognized in Nevada (Ritterbush et al. 2014), Peru

*Present Address: Department of Earth Sciences, University of Cambridge, Cambridge, U.K.
†Present Address: California Institute of Technology, Division of Geological and Planetary Sciences, Pasadena, California, U.S.A.

Published Online: October 2022
 1527-1404/22/092-896

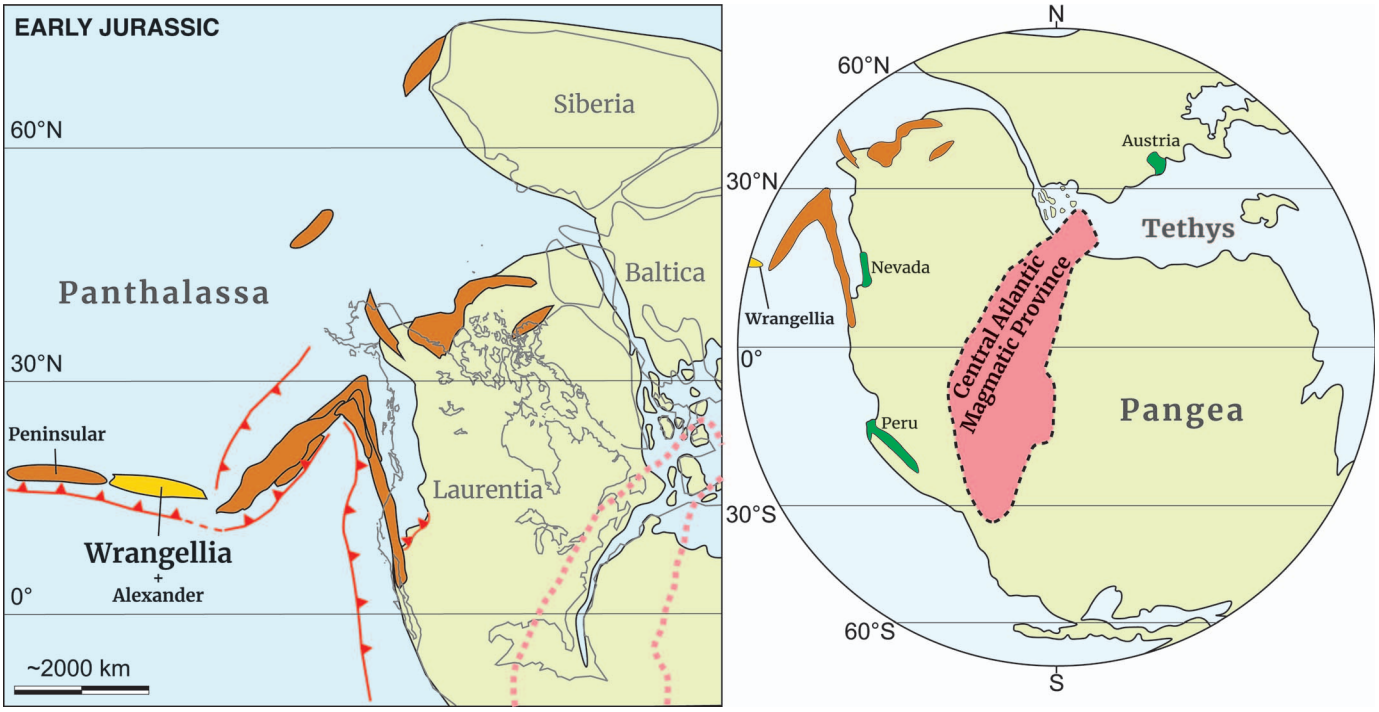

FIG. 1.—**A)** Paleogeographic map of eastern Panthalassa (modified from Fig. 18 in Nelson et al. 2013, using Blackburn et al. 2013, and Krencker et al. 2015). **B)** Paleogeographic map of the Pangean hemisphere showing the extent of the Central Atlantic Magmatic Province, eastern Panthalassan terranes (orange and yellow), and known glass-ramp records (green) from the margins of Pangea (modified from Ritterbush 2019).

(Ritterbush et al. 2016), and Austria (Delecat et al. 2011). Glass ramps are continental margins characterized chiefly by accumulations of siliceous skeletal sediments (Gates et al. 2004). Weathering of CAMP basalts and the resulting increase in oceanic silica concentration are thought to have promoted the transition to glass ramps (Ritterbush 2019).

Evidence for a decline in carbonate-rich and an increase in biosiliceous sedimentation across the Triassic–Jurassic boundary interval is currently limited to the continental margins of Pangea (Fig. 1; Ritterbush 2019) with no data from the open Panthalassan Ocean. Additionally, many of the Tethyan neritic records of the Triassic–Jurassic boundary interval, though relatively abundant and easily accessible, are known to contain significant hiatuses (Hillebrandt et al. 2013; Ritterbush et al. 2014). The paucity of marine sections across the Triassic–Jurassic boundary (see also Fig. 1 in Peters and Foote 2002), particularly from outside the Tethyan region, has limited our understanding of the impact of igneous activity of CAMP and the end-Triassic mass extinction on biogenic sedimentary systems.

To address these issues, we present here new sedimentary and stratigraphic data from the Upper Triassic to Lower Jurassic McCarthy Formation at Grotto Creek (Wrangell Mountains, southcentral Alaska). The McCarthy Formation represents a biostratigraphically complete upper Norian (Cordilleranus Zone) to upper Hettangian (Mineralense–Rursicostatum zones) section deposited on the Wrangellia terrane—then, an isolated deepwater oceanic plateau in the tropical Panthalassan Ocean (Jones et al. 1977; Trop et al. 2002; Caruthers et al. 2022). The formation represents a unique oceanic deepwater perspective on sedimentation on Triassic–Jurassic ramps. The aim of this project was to study the facies of the McCarthy Formation at Grotto Creek to reconstruct: i) the processes responsible for sedimentation in the outer-ramp depositional environments of the Wrangellia plateau and ii) the controls on Late Triassic to Early Jurassic tropical deepwater sedimentation in the Panthalassan Ocean.

In this manuscript we: i) present further evidence in support of a long Rhaetian, ii) present Panthalassan evidence for a facies change from siliceous carbonate-ramp to siliceous, or "glass," ramp at the Triassic–Jurassic boundary; and, as far as we are aware, iii) present the first record of contouritic sedimentation in the lowermost Jurassic.

GEOLOGICAL SETTING

Southcentral Alaska consists of three fault-bounded allochthonous composite terranes (Jones et al. 1977; Hillhouse and Gromme 1984; Trop et al. 2002; Trop and Ridgway 2007). The Wrangellia composite terrane abuts the Yukon–Tanana composite terrane to the north along the Denali fault and the Southern Margin composite terrane to the south along the Border Ranges fault. The Wrangellia composite terrane consists of three tectonostratigraphic terranes: the Alexander, Peninsular, and Wrangellia terranes (Plafker and Berg 1994; Nokleberg et al. 2000), which are thought to have become juxtaposed during the late Paleozoic (Plafker et al. 1989). Unlike the other two terranes, which form continuous units, the Wrangellia terrane consists of a northern (Alaska) and a southern (British Columbia) block that share a similar Triassic lithological sequence (Jones et al. 1977).

Paleomagnetic and geological data suggest that during the Late Triassic the Wrangellia composite terrane was located near the equator (~ 15° N), several thousand kilometers south of its present position (Fig. 1; Jones et al. 1977; Hillhouse and Gromme 1984; Hillhouse and Coe 1994; Plafker and Berg 1994; Butler et al. 1997). The composite terrane moved northward and accreted onto the western margin of Laurasia some time during the Middle Jurassic–Late Cretaceous (Csejtey et al. 1982; McClelland et al. 1992; Nokleberg et al. 2000).

The Triassic of northern Wrangellia is dominated by the Nikolai Greenstone, which near McCarthy, Alaska, consists of at least 3,000 m of basalt emplaced during a single phase of subaerial tholeiitic volcanism 230–225 Ma ago (Greene et al. 2010; Shellnutt et al. 2021). The Nikolai Greenstone is underlain by discontinuous lenses of Ladinian (Middle Triassic) black cherts and mudstones (MacKevett 1978); it is overlain nonconformably by the Chitistone Limestone (Fig. 2), which consists of thick to very thick (0.5–5 m) beds of limestone with subordinate dolostone

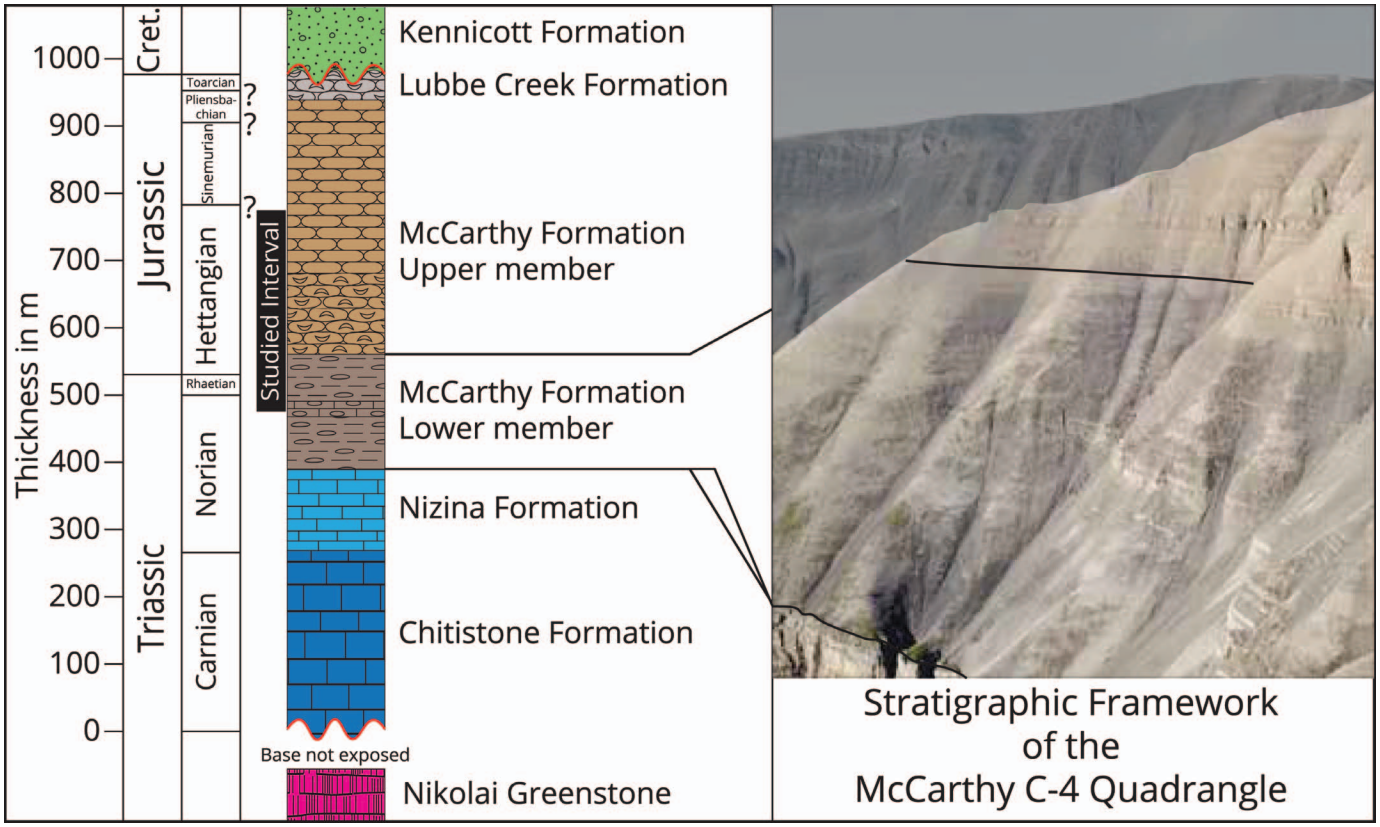

FIG. 2.—Stratigraphic framework of the Triassic–Jurassic of the Wrangell Mountains, based on MacKevett (1970a), Trop et al. (2002), Witmer (2007), and Caruthers et al. (2022). The photograph of the Grotto Creek section was taken toward the south and shows the member boundary of the McCarthy Formation, which is marked by a color change in the landscape. On a smaller scale, the McCarthy Formation shows alternations between cliff-forming and slope-forming intervals, which correspond to the facies associations of this study.

and chert nodules (Armstrong et al. 1969). The lowermost part of the formation consists of micritic limestones that locally contain evaporites (Armstrong et al. 1969). This formation is overlain by the Nizina Limestone (Fig. 2), which consists of medium to thick (15–90 cm) beds of limestone with subordinate chert lenses and nodules and rare grains of dolomite (Armstrong et al. 1969). This calcareous succession of the Chitistone and Nizina limestones is approximately 1,100 m thick and was deposited from the Carnian to the late Norian.

The bulk of the Chitistone and Nizina limestones accumulated in shallow-water shelf environments. The lowermost Chitistone Limestone contains microbialites and evaporites and was deposited in supratidal to intertidal environments. The upper Chitistone and Nizina limestones accumulated in more open shallow-water shelf environments, including high-energy ooidal shoals, but also contain more restricted lagoonal deposits (Armstrong et al. 1969). Corals are found at the transition from the Chitistone Limestone to Nizina Limestone, but reefs never developed at the platform edge (Armstrong et al. 1969; Caruthers and Stanley 2008).

In the Norian, the carbonate platform of Wrangellia drowned and approximately 900 m of siliceous mudstones accumulated until the Sinemurian (or Pliensbachian). These sediments form the McCarthy Formation, named after McCarthy Creek by Rohn (1900), which is exposed across the Wrangell Mountains of southcentral Alaska (MacKevett 1978). Exploration (Schrader and Spencer 1901; Moffit and Capps 1911; Martin 1916; Moffit 1930, 1938) and mapping (MacKevett 1963, 1970a, 1970b, 1972, 1974, 1978; MacKevett and Smith 1972a, 1972b; MacKevett et al. 1978; Winkler and MacKevett 1981) throughout the 20th century paved the way for current environmental interpretations of this unit within the context of the displaced terranes of the North American Cordillera (Jones et al. 1977; Trop et al. 2002; Trop and Ridgway 2007). The formation has been interpreted to represent the distal environments of a carbonate ramp which became submerged below storm wave base during post-volcanic thermal subsidence of the oceanic plateau (Armstrong et al. 1969; Witmer 2007).

The McCarthy Formation is overlain by the Pliensbachian–Toarcian shallow-marine Lubbe Creek Formation (Fig. 2), which consists of ~ 50 m of spiculite and subordinate coquina. This succession is suggested to represent a forced regression. The Lower Jurassic succession ends with a disconformity representing a hiatus of 10–15 Myr (MacKevett 1969; Trop et al. 2002).

Triassic–Jurassic Paleogeography of the McCarthy Ramp

We constructed isopach maps for the Chitistone Limestone, Nizina Limestone, and McCarthy formations based on reported thicknesses in the USGS quadrangle maps of the area (see supplementary materials, Fig. S1). The orientation of the isopachs is approximately northwest–southeast (Fig. S1) and probably reflects the depositional strike of the ramp. The thickness pattern of the three formations is consistent with a depositional dip toward the west-southwest: the Chitistone Limestone Formation, which represents the shallowest part of the ramp (Armstrong et al. 1969), thickens toward the northeast, whereas the Nizina Limestone and the McCarthy formations, which represent deeper environments, are thicker in the southwest. Although this thickness pattern is consistent with observations made by Martin (1916), the interpretation of a depositional dip toward the west-

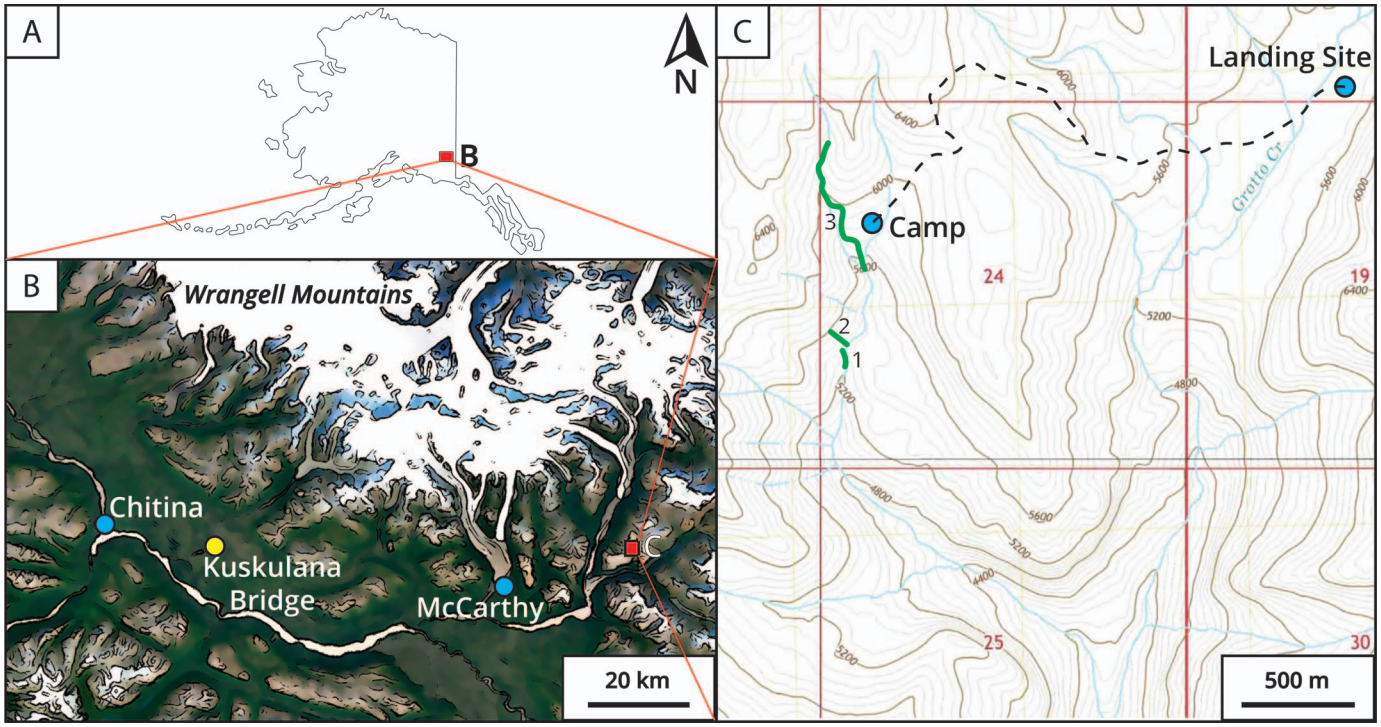

FIG. 3.—Location of the Grotto Creek section relative to **A)** Alaska, **B)** the Chitina River Valley, and **C)** Chitistone Mountain. In Part C, the dotted line is the hiking route from the landing site at the headwaters of Grotto Creek to the section. The green lines mark the three sub-sections of this study. Basemap: USGS non-ortho US Topo 2017.

southwest differs from Trop et al. (2002), who suggested that the ramp dipped toward the northeast.

MATERIALS AND METHODS

The Grotto Creek Section

We studied a section of the McCarthy Formation (Fig. 2) during two field seasons, in 2017 and 2019, along an unnamed tributary of Grotto Creek, ~ 25 km east-northeast of McCarthy, in southcentral Alaska (Fig. 3). This section was originally described in the unpublished bachelor's thesis of Witmer (2007). Caruthers et al. (2022) recently published biostratigraphic and chemostratigraphic (i.e., organic carbon isotope) data, as well as U-Pb age dates from bentonites, from the Triassic–Jurassic boundary interval of Grotto Creek (see Fig. S2).

We studied ~ 290 m of stratigraphy, spanning the upper part of MacKevett's (1963, 1978) lower member and the lower part of his upper member of the McCarthy Formation (Figs. 2, 4). Recent work has placed the Triassic–Jurassic boundary 26.4 m below the base of the upper member of the McCarthy Formation (Caruthers et al. 2022). The base of the upper member is at 58.8 m in our composite section (Fig. 4). Following Caruthers et al. (2022), the 0 m datum of our composite section is placed at the base of an easily recognizable 5-cm-thick bentonite just below the Norian–Rhaetian boundary. We grouped the facies of the McCarthy Formation into four facies associations (Table 1) and calculated approximate linear sedimentation rates for the Rhaetian and Hettangian at Grotto Creek (Table 2).

We measured, described, and sampled three sub-sections (Fig. 3). The lower section (base at 07V 423,246 m, 6,819,740 m; NAD 83) is 26.28 m thick and was studied along the creek. The top of the lower section is a ~ 0.5-m-thick dolerite sill, which also forms the base of the middle section (07V 423,251 m, 6,819,839 m). The middle section is 70 m thick and was studied by climbing the slope. The uppermost ~ 34 m of this section overlaps with the upper section. We correlated these two sub-sections using prominent marker beds. The upper section is ~ 227 m thick and was studied along the creek (from 07V 423,340 m, 6,820,172 m to 423,156 m, 6,820,894 m). We collected 107 samples: 62 lower member rocks and 45 upper member rocks (Table S2).

Analytical Methods

Fifty bulk samples were analyzed qualitatively for their mineral composition (see Table S2). These samples were reduced to a fine powder and front-sideloaded onto PMMA sample holders with a cavity diameter of 25 mm. Bulk mineral compositions were determined by running the samples on a Bruker D8 Advance X-ray diffractometer with a θ/θ goniometer. We used a primary Soller slit of 2.5° and a variable divergence slit—resulting in a constant irradiated length of 20 mm, a motorized anti-scatter screen, and an antiscatter slit of 18 mm. X-ray powder diffraction patterns were recorded from 3 to 75 °2θ, in steps of 0.02°, counting for 0.85 s per step, using Cu-$K\alpha$ radiation (40 kV, 40 mA). Samples were continuously spun (0.25 Hz) during measurement.

Thirty-five samples were analyzed for their elemental composition (see Table S2). These samples (~ 10 g) were powdered for 120 s and pressed into tablets with a diameter of 35 mm using a Herzog HP-PA. Bulk elemental compositions were measured using an ARL Perform'X X-ray fluorescence (XRF) spectrometer. The sum of the wt% of the major elements (Al_2O_3, CaO, Fe_2O_3, K_2O, MgO, MnO, Na_2O, P_2O_5, SiO_2, and TiO_2) was on average ~ 84%.

Grain-size distributions were determined for the insoluble residue of samples using a Malvern Mastersizer 2000 (see Table S2). The samples are siliceous and resist disaggregation. For this reason, we crushed them to the size of coarse sand using a hammer before chemical pretreatment. The crushed samples were placed in beakers with 3M HCl and stir bars on a magnetic stirrer at 70 °C for four days. After neutralizing the remaining acid, we added 12% H_2O_2 to the samples and kept stirring them at room

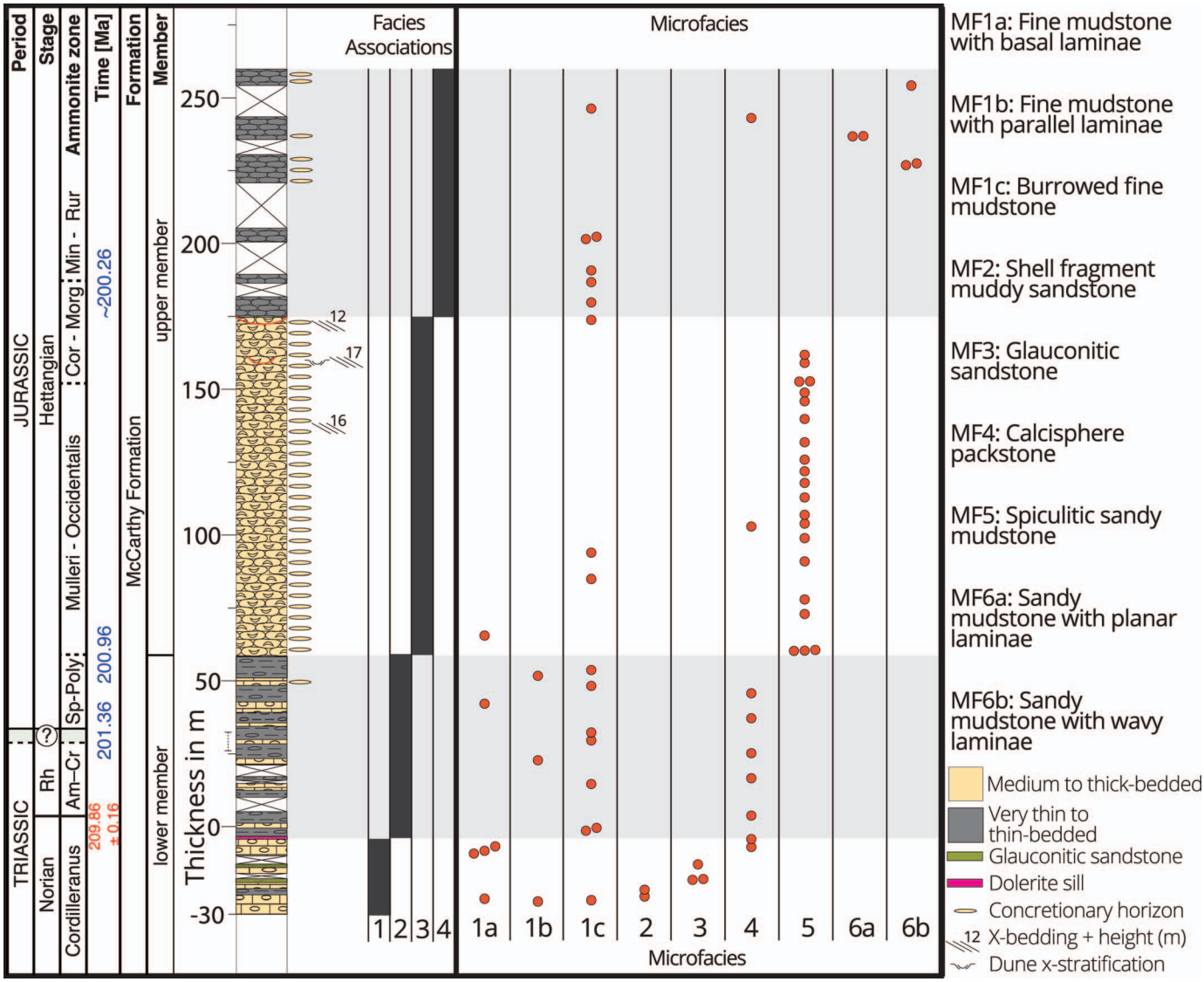

FIG. 4.—Schematic log of the studied interval, which shows an alternation between cliff-forming thicker-bedded intervals (FA1 and FA3), interpreted as lobe complexes, and slope-forming thinner-bedded intervals (FA2 and FA4; gray shading), interpreted as sediment-starved outer-ramp environments. The upper member is more siliceous than the lower member. Following Caruthers et al. (2022), we used a bentonite dated at 209.86 Ma as the 0 m datum. Younger ages are based on ammonite zones, their approximate correlations to European ammonite zones, and ages from Hesselbo et al. (2020).

TABLE 1.—*Overview of the facies associations of the McCarthy Formation.*

		Facies Associations	Description	Common Microfacies		Environment
upper member	slope-forming	FA4	Thin- to medium-bedded siliceous mudstones alternating with medium- to thick-bedded laminated calcareous cherts.	MF1c MF6a MF6b	Burrowed fine mudstone Sandy mudstone with planar laminae Sandy mudstone with wavy laminae	Sediment-starved outer ramp of a glass ramp
	cliff- forming	FA3	Medium- to thick-bedded spiculitic cherts and concretionary horizons.	MF5	Spiculitic sandy mudstone	Glass-ramp lobe complex
lower member	slope-forming	FA2	Thin-bedded and subordinately thick-bedded siliceous mudstones, calcareous cherts, and limestones.	MF1b MF1c MF4	Fine mudstone with parallel laminae Burrowed fine mudstone Calcisphere packstone	Sediment-starved outer-ramp of a siliceous carbonate ramp
	cliff-forming	FA1	Medium- to thick-bedded siliceous mudstones, calcareous cherts, shell-fragment limestones, and very thin to thin partings.	MF1a MF2 MF3	Fine mudstone with basal laminae Shell fragment muddy sandstone Glauconitic muddy sandstone	Siliceous carbonate ramp lobe complex

TABLE 2.—*Thicknesses and average linear sedimentation rates for intervals of the Rhaetian and the Hettangian. The lower sedimentation rate of the Rhaetian part of FA2 is attributed to the inferred presence of hiatuses caused by phases of carbonate dissolution resulting from ocean acidification. The higher sedimentation rate of the Mulleri–Morganense zones represents the onset of sediment shedding, which resulted in FA3, and a recovery of biogenic sediment production on a glass ramp. For the height of the Rhaetian–Hettangian boundary, we chose the middle of the Triassic–Jurassic boundary interval in Caruthers et al. (2022) (see also Fig. S2). The duration of the Rhaetian is based on Caruthers et al. (2022). Durations of the Hettangian ammonite zones are based on ages from Hesselbo et al. (2020), using approximate correlations of the North American ammonite zones to their European equivalents (cf. Figs. 4, S3).*

Stage	Facies Association	Position of Boundaries	Thickness	Duration	Average Un-Decompacted Sedimentation Rate
Hettangian Mulleri–Morganense zones	mostly FA3	58.8–187.3 m	128.5 m	~ 700 ka	~ 184 m/Myr
Hettangian Spelae–Polymorph zones	FA2	32.4–58.8 m	26.4 m	~ 400 ka	~ 66 m/Myr
Rhaetian	FA2	3.6–32.4 m	28.8 m	~ 8 Ma	~ 3.6 m/Myr

temperature, while the organic matter oxidized. When the reaction had visibly ceased, the samples were heated to 90 °C to allow any remaining H_2O_2 to react. Despite this pretreatment, only 25 samples disaggregated fully and could be measured using laser particle-size analysis (see Table S2). For this reason, we complemented these results with grain-size analysis of 44 samples in thin section using ImageJ (see below). We measured the insoluble residues using a protocol modified from Sperazza et al. (2004). Before each measurement, we added 25 mL of a dispersing solution (44.6 g $Na_4P_2O_7{\cdot}10H_2O$ and 4.24 g Na_2CO_3 in 1 L deionized water) and applied 60 s of ultrasound with a maximum tip displacement of 4 µm. The grain-size distribution was calculated using a refractive index of 1.544 and an absorption index of 0.9. We remeasured a sub-sample to check for machine precision and we re-sub-sampled and measured two samples to check for operator precision (see data in Supplemental Materials).

Petrography and Microfacies Analysis

We produced ~ 20-µm-thick polished thin sections of 66 samples (Tables S1 and S2). We studied them in plane- (PPL) and cross-polarized light (XPL) using a Zeiss Axio or a Leica DM 2700 P microscope. Micrographs were taken using a Zeiss Axiocam 305 Color camera or a

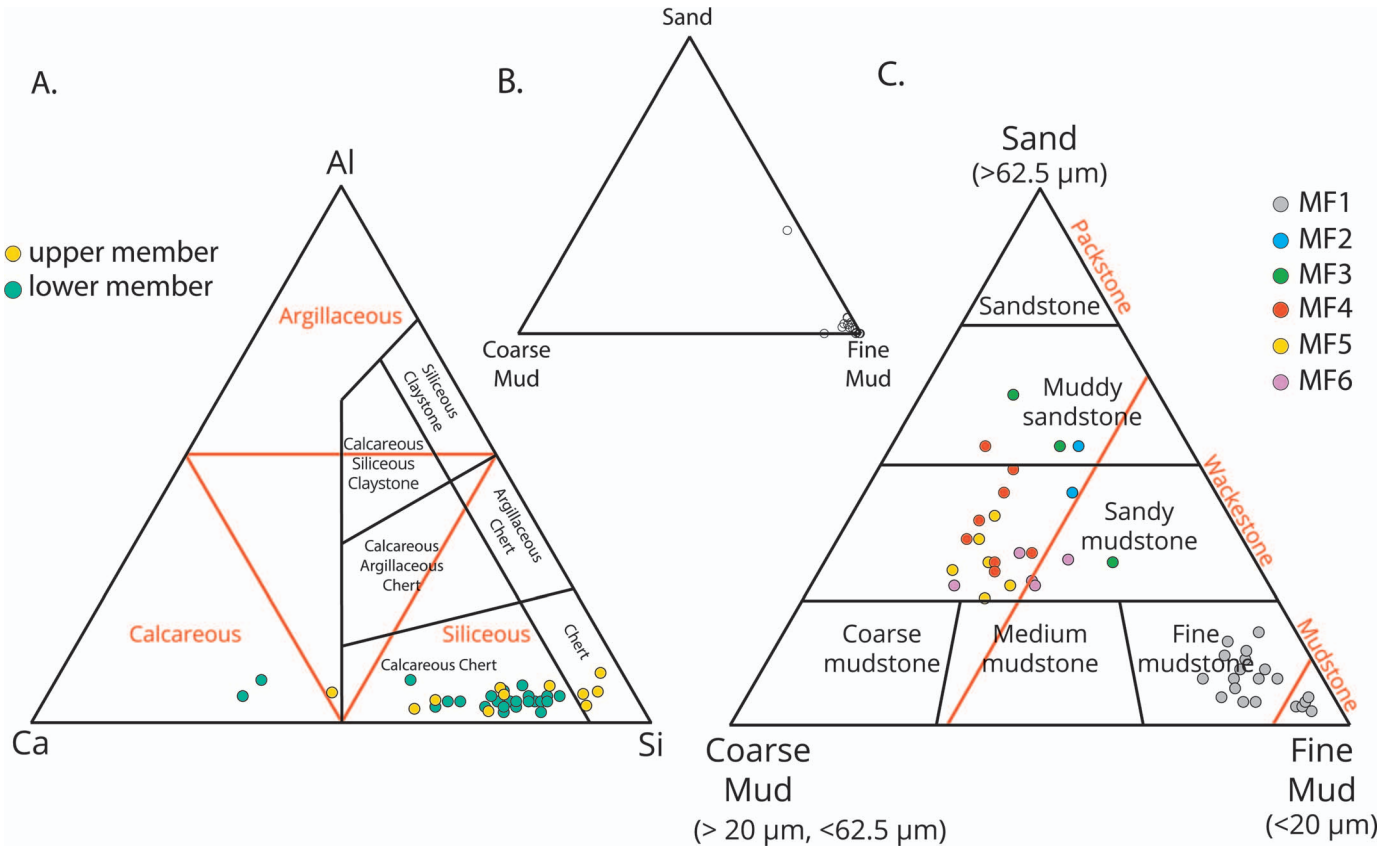

FIG. 5.—The facies of the McCarthy Formation in three ternary diagrams. **A)** Compositional ternary diagram combining Lazar et al. (2015) (in red) and Jones and Murchey (1986) (in black). Most samples are siliceous mudstone and calcareous chert. The calcareous samples are rich in shell fragments and occur only in the lower member, whereas bedded cherts are often spiculitic and occur only in the upper member. The Al% is low, which shows that the total lithogenic component is small. **B)** Grain-size ternary diagram based on laser grain-size analysis of the insoluble residue of samples. Most of the insoluble residue is microcrystalline. **C)** Textural ternary diagram, based on thin sections, combining a modification of Lazar et al. (2015) (in black) with Dunham (1962) (in red). The mudstone–wackestone boundary corresponds to 90% fine mud, and the wackestone–packstone boundary is placed at 35% fine mud, which is the approximate upper limit for grain-supported fabrics.

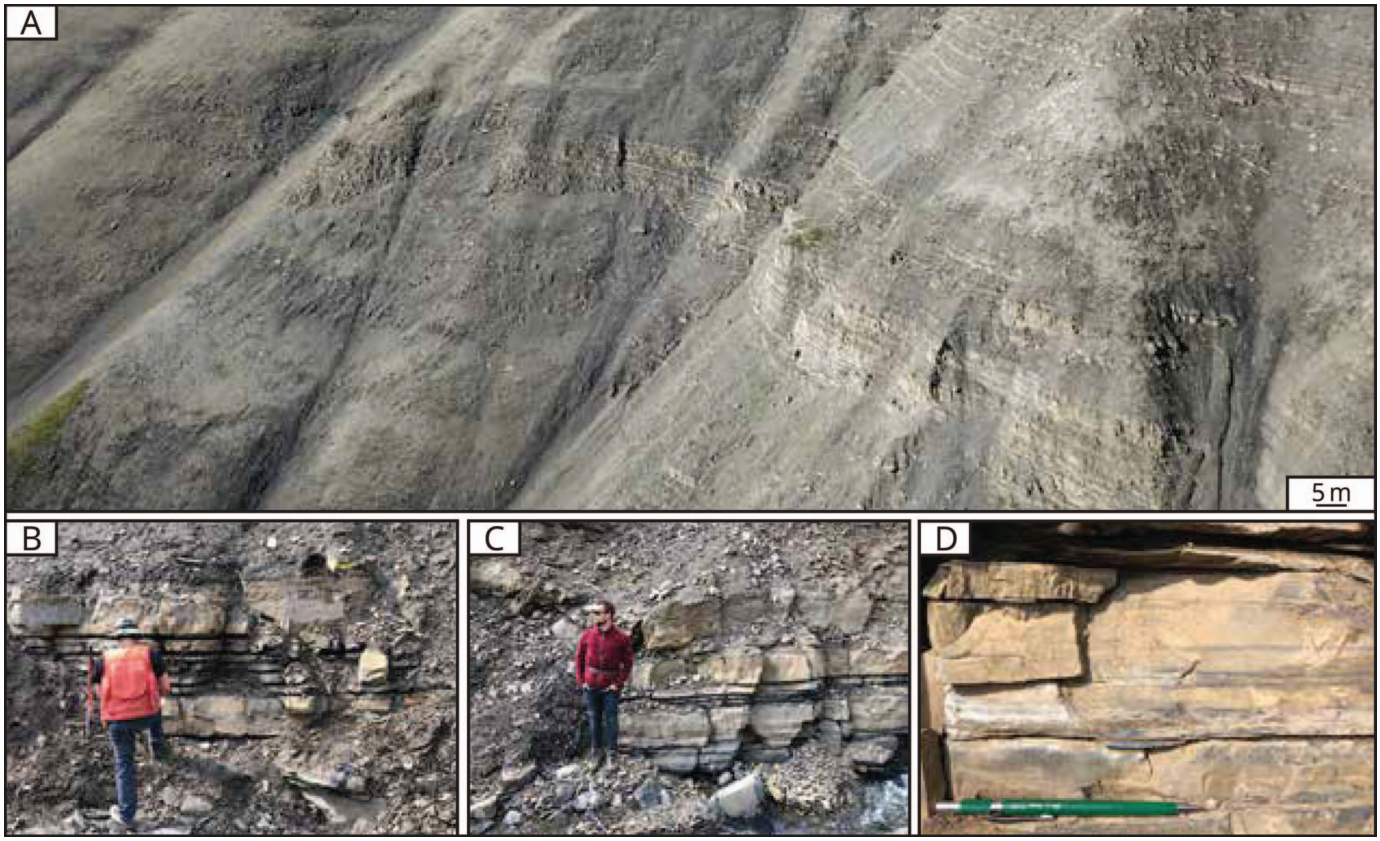

FIG. 6.—Facies association 1, which is interpreted as an outer-ramp lobe complex on a siliceous carbonate ramp. **A)** Photograph taken toward the southwest. FA1 is cliff-forming and appears to pinch toward the south, which is interpreted to represent the geometry of the lobe complex. **B**, **C)** FA1 consists of medium to thick beds and thin partings. Thicker beds sometimes contain sand-size shell fragments (MF2) or glauconite (MF3). Parts B and C show the same bedset: bed thickness changes laterally over ~ 10 m, which is interpreted to represent the geometry of lobe elements. **D)** Laminated bed with irregular basal contacts consisting of fine mudstone with basal laminae (MF1a).

Leica MC170 HD. We used reflected light to determine the composition of opaque materials.

Because most samples are fine grained, we adopted an approach modified from Lazar et al. (2015) to capture textural variability adequately. Here, we define fine mud as grains smaller than 20 μm and coarse mud as grains between 20 and 62.5 μm (see Fig. 5C). The reason for this modification is that 20 μm corresponds to the average thickness of our thin sections. As a result, grains smaller than 20 μm appear as a dark matrix under the microscope, which sets them apart from coarser transparent grains. Ten to twenty micrometers seem to separate the cohesive mud and sortable silt of McCave et al. (1995), as well as (aggregate) grains that travel as bedload from grains that are brought into suspension by turbulence at the threshold of sediment movement. Coincidentally (or not), 20 μm is the boundary between mud and grains in the original Dunham classification (Dunham 1962).

The amount of fine mud, coarse mud, and sand was estimated using ImageJ by Fiji software. For this analysis, we selected 44 representative thin sections (see Tables S1 and S2) and used scans produced using a Leica M165C stereomicroscope. These scans, with a resolution of ~ 7 μm/px, allowed for the study of relatively large representative areas of the thin sections. Images were processed as follows: First, grains with an area smaller than 4 px were excluded to avoid noise. This size corresponds to grains with a nominal diameter of 19.7 μm or finer. Then, a brightness threshold was used to differentiate fine mud and coarser grains. This resulted in binary images that included all grains coarser than 20 μm. The binary images were then filtered to differentiate coarse mud ($\geq$ 20 μm, $<$ 62.5 μm) and sand grains ($\geq$ 62.5 μm).

For a few samples with carbonate cement, we did not use the brightness threshold, because the cement and the grains have a similar brightness under the microscope. For such samples, the grain-size distribution was assessed by comparing them with other samples and to visual charts (Baccelle and Bosellini 1965).

In the microfacies descriptions (see Supplemental Materials), we adopted the semiquantitative terminology of Macquaker and Adams (2003): dominating ($\geq$ 90%), rich (50–90%), and bearing (10–50%). Additionally, bioturbation intensity was quantified using the bioturbation index of Droser and Bottjer (1986). The thickness of beds and laminae were described using the terminology proposed by Campbell (1967).

RESULTS AND INTERPRETATION

Facies Characterization

The facies of the McCarthy Formation are siliceous (Fig. 5A): of the 35 samples we analyzed using XRF (Table S2), 32 are siliceous mudstones and 2 are calcareous mudstones (*sensu* Lazar et al. 2015); of the 32 siliceous mudstones, 28 are calcareous cherts (*sensu* Jones and Murchey 1986) and 4 are siliceous enough to be called cherts (Fig. 5A). Siliceous samples contain radiolarians and/or spicules. Microcrystalline quartz is a significant siliceous phase in the McCarthy Formation, which is reflected by the fine textures of the insoluble residue of samples (Fig. 5B): 23 of 25 samples have a modal grain size below 5 μm. Calcite in calcareous samples

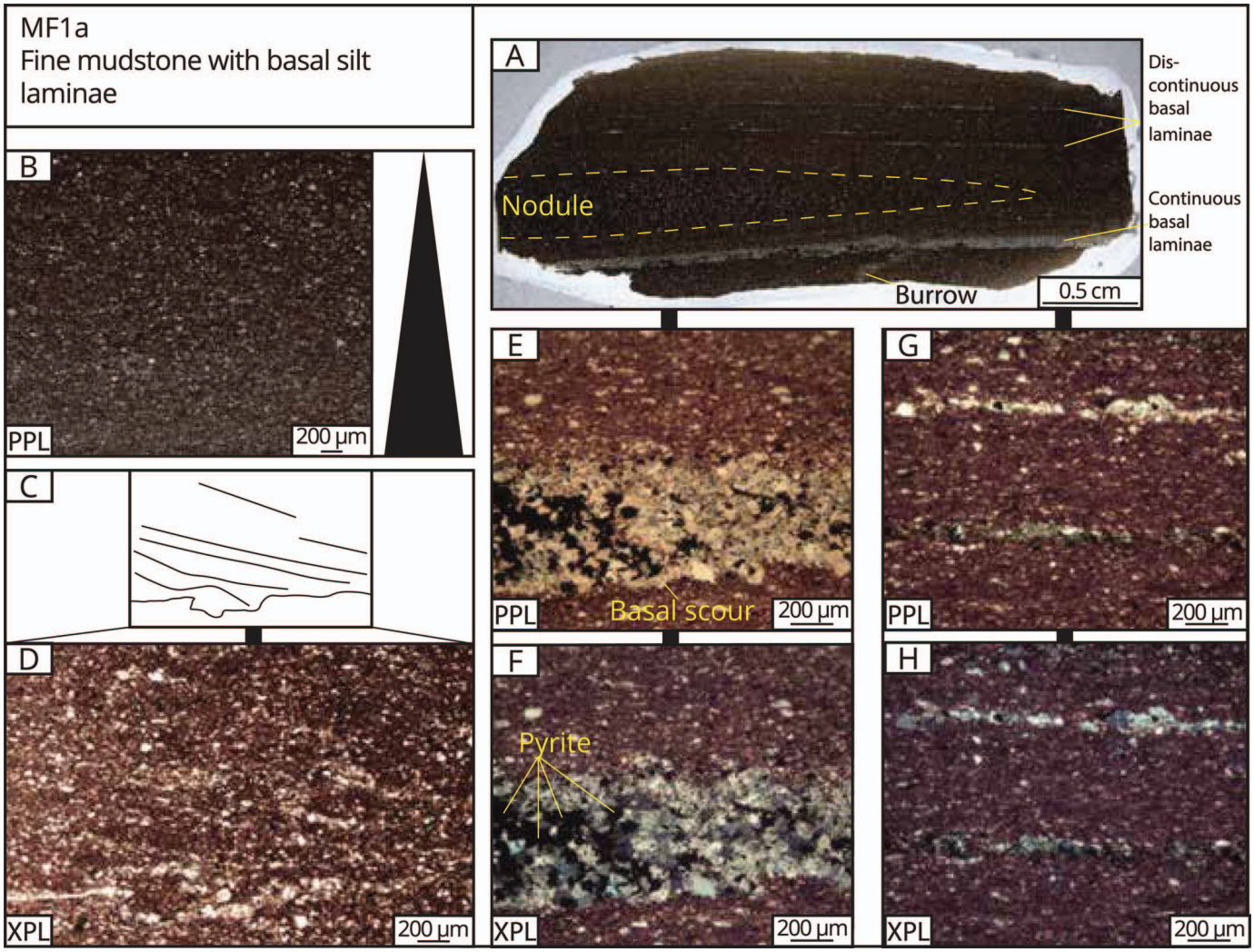

FIG. 7.—MF1a: fine mudstone with basal silt laminae, interpreted to represent fine-grained turbidity currents. This microfacies shows evidence for bedload transport and waning currents. **A)** Thin-section overview. **B)** Normal grading in the fine mud. **C**, **D)** Laterally discontinuous set of cross-laminae that downlap tangentially onto a basal scour. **E**, **F)** Micrograph of continuous basal laminae, which are well cemented and bear pyrite grains. **G**, **H)** Micrograph of discontinuous basal laminae, which are a few grains thick and lenticular, pinching out and reappearing on the scale of millimeters.

is present as sparite cement, shallow-water skeletal grains, pelagic calcispheres, or carbonate mud (micrite).

Overall, the upper member is more siliceous than the lower member: In the lower member, chert occurs only in nodules, and bedded cherts are present only in the upper member (Fig. 5A). In general, the quartz/calcite intensity ratio (XRD) is higher in the upper member than in the lower member (Fig. S4). In thin section, the upper member has a higher abundance of siliceous spicules, whereas the lower member contains more calcareous skeletal grains and micrite.

In addition to quartz and calcite, the typical mineral assemblage of the mudstones of the McCarthy Formation consists of albite, ankerite, apatite, dolomite, hematite, muscovite, and pyrite (Fig. S4). The total amount of aluminum in the rocks is low (2–9%, average 4%; Fig. 5A), which indicates that their terrigenous component is small.

Facies Associations

The four facies associations in the studied interval are described below and summarized in Table 1.

Facies Association 1.—Facies association 1 is an ~ 26-m-thick cliff-forming succession of medium to thick beds of siliceous mudstone, calcareous chert, skeletal limestone, and very thin to thin partings of fissile mudstone (Fig. 6). These rocks are part of the lower member of MacKevett (1963). FA1 is an association of microfacies 1–3 (Figs. 7–11; see below). The contacts between beds are sharp and can be slightly irregular (Fig. 6D). Both the partings and most thicker beds are medium gray to black when fresh and consist of very thin to thin beds of fine siliceous mudstone (MF1). Some of these fine mudstones have very thin basal laminae (Fig. 7), whereas others are burrowed (Fig. 9). Nodules of chert and apatite are common in the siliceous mudstones (Fig. 7A). Some thin to thick beds are coarser and contain skeletal sand (Fig. 10) or glauconite (Fig. 11). Common macrofossils are *Monotis*, *Heterastridium*, and various ammonoids indicating a late Norian age (Cordilleranus Zone; see Caruthers et al. 2022). The thickness of bedsets was observed to change laterally over a distance of ~ 10 m (Fig. 6B, C). On a larger scale, in the Grotto Creek section, FA1 pinches out toward the south (Fig. 6A).

Facies Association 2.—Facies association 2 is an ~ 70-m-thick slope-forming succession of predominantly dark, thin-bedded, fine siliceous

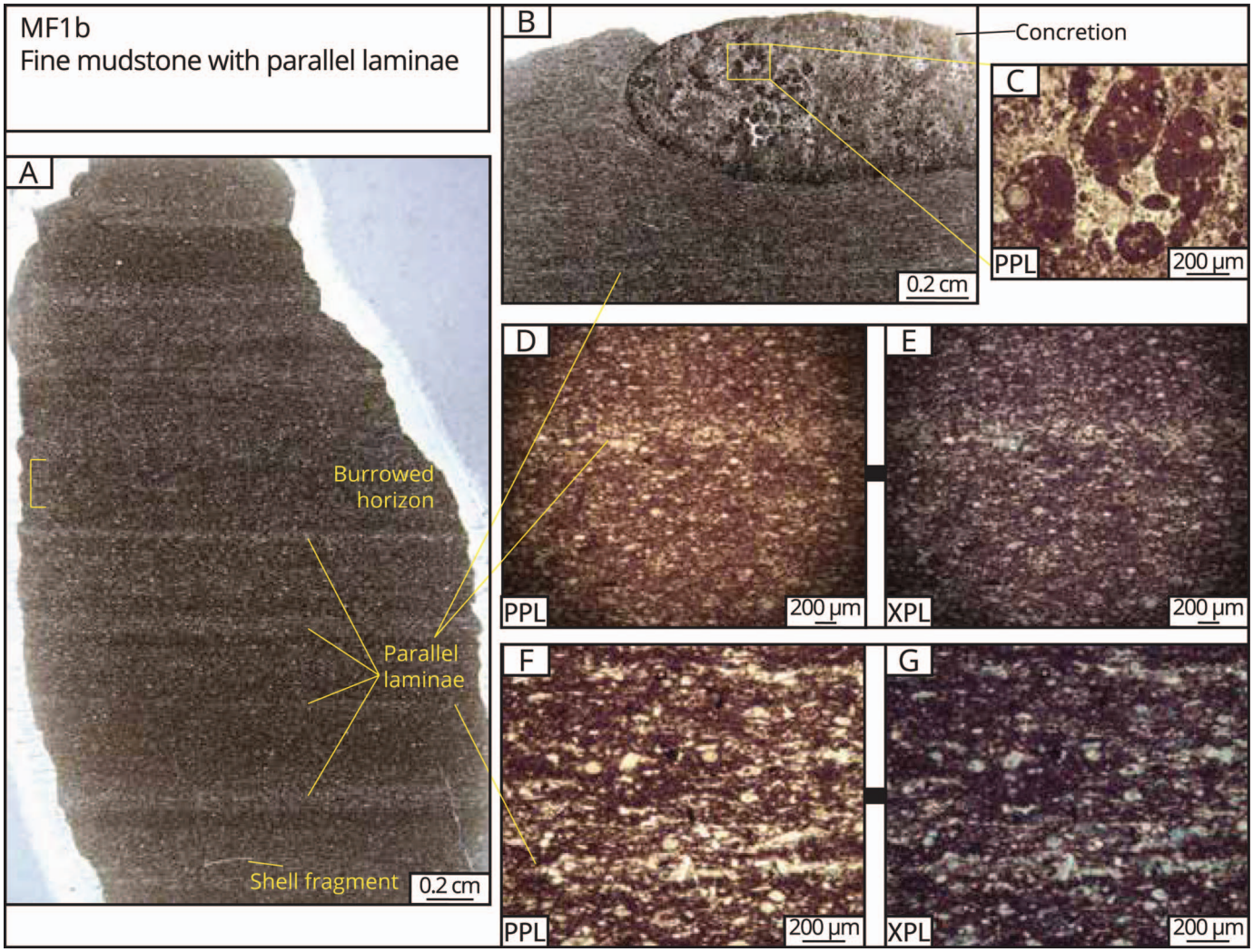

FIG. 8.—MF1b: fine mudstone with parallel laminae, interpreted to represent suspension settling. **A)** Thin-section overview. **B**, **C)** Concretion in which the primary peloidal texture of the fine mud is preserved. **D**–**G)** Micrographs of laminae showing gradational contacts. Coarse laminae are typically more well cemented than the surrounding fabric.

mudstones and subordinately buff-colored medium to thick beds of siliceous mudstone, calcareous chert, and limestone (Fig. 12). FA2 contains several ash layers (see Caruthers et al. 2022). These rocks are part of the lower member of MacKevett (1963). FA2 is an association of microfacies 1 and 4 (Figs. 7–9, 13; see below). The predominant fine siliceous mudstones contain parallel laminae (Fig. 8) or are burrowed (Fig. 9). The buff-colored medium to thick beds consist of calcisphere packstones (Fig. 13) or occasionally of fine siliceous mudstones (Figs. 8, 9). Some of the fine mudstones contain small (~ 1–2 cm in diameter) carbonate concretions or chert nodules, which are internally rich in sand-size peloids (Fig. 8B). In the upper ~ 40 m of FA2, both thin and medium to thick beds are sometimes laminated. A few siliceous mudstones in the upper part of FA2 bear outsized shell fragments or plant material (see Witmer 2007). The contacts between the different beds may be sharp or gradational. The base of FA2 contains several syndepositional folds with a maximum height of ~ 12 m (Fig. 12B).

Facies Association 3.—Facies association 3 is an ~ 120-m-thick cliff-forming succession of medium- to thick-bedded dark spiculitic cherts and buff-colored carbonate concretionary horizons (Figs. 14, 15). These rocks are part of the upper member of MacKevett (1963). FA3 is an association of microfacies 1c and 5 (Figs. 9, 16; see below). The concretionary horizons and the cherts are similar in texture, as both cherts and concretions consist of spiculitic sandy mudstone (Fig. 16). The difference between cherts and concretionary horizons is that the cherts contain more siliceous mud (Fig. 16G), whereas the concretions contain more sparite (Fig. 16C–F). The concretions are ~ 30 cm thick and have a horizontal diameter of ~ 60 cm. They often coalesce laterally to form continuous horizons with wavy contacts (Fig. 14B). In several concretionary horizons, we observed sigmoidal surfaces that downlap tangentially onto the underlying bedding plane (Fig. 14C).

The uppermost ~ 50 m of FA3 shows sets of large-scale low-angle cross-stratification with heights of 12–17 m and dip angles relative to the overall bedding of 6–8° (Fig. 15; Heinhuis 2020). The concretions in the intervals with large-scale low-angle cross-stratification are ~ 8 cm tall and 10–20 cm wide, that is, smaller than in the rest of FA3 (Fig. 14). The sets of large-scale low-angle cross-stratification are associated with channel-forms with a depth of ~ 3 m and a width of ~ 15 m (Fig. 15A). The channelforms cut into the sets of large-scale low-angle cross-stratification and, in turn, are filled by cross-stratified bedsets (Fig. 15C). The upper boundary of FA3 is an erosional surface displaying larger channelforms that have a depth of 5–10 m and a width of ~ 30 m (Fig. 15C).

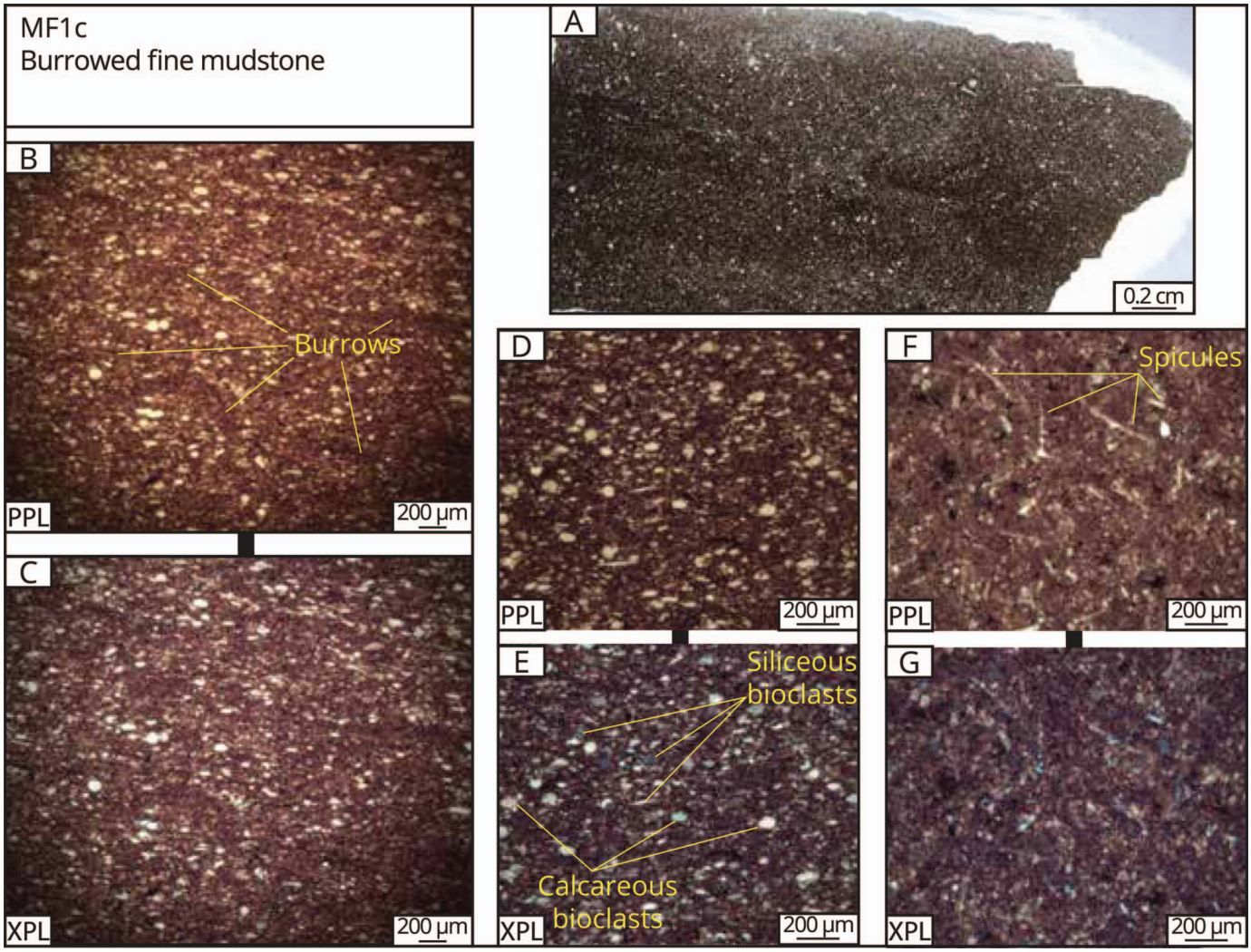

FIG. 9.—MF1c: burrowed fine mudstone. Some beds of this microfacies represent background sedimentation, whereas others represent more dynamic processes. **A)** Thin-section overview. **B**, **C)** Micrograph with recognizable burrows, which shows that the fabric has not been completely homogenized by bioturbation. Some of the burrows are *Phycosiphon* sp. **D**, **E)** Many fine mudstones contain both siliceous microfossils, such as radiolarians, and calcareous microfossils, such as calcispheres. **F**, **G)** An anomalous sample from the lower member (FA1) bearing reworked spicules, which are a subordinate bioclast in the lower member.

Facies Association 4.—Facies association 4 is an ~ 85-m-thick slope-forming succession of very thin to medium beds of siliceous mudstone alternating with medium to thick beds of laminated calcareous chert (Fig. 17). FA4 contains several ash layers. These rocks are part of the upper member of MacKevett (1963). FA4 is an association of microfacies 1c and 6 (Figs. 9, 18; see below).

The siliceous mudstones have a dark olive to black color (Fig. 17B), are burrowed (Fig. 9), and are typically richer in chalcedony than the mudstones of the lower member. The upper half of FA4 contains indurated medium to thick beds that appear every 1 to 10 m (Fig. 17A, D). These thicker beds are buff-colored calcareous cherts that consist of laminated sandy mudstone (Fig. 18); they are sometimes concretionary. Some of these thicker beds exhibit bigradational sorting—a vertical transition of reverse to normal grading within the same bed (Figs. 17C, 18A–F). Other thicker beds contain very thin wavy laminae (Fig. 18G–K).

Microfacies

We defined nine microfacies (Figs. 7–11, 13, 16, 18), which we describe in Table 3 (see also Supplemental Materials) and interpret below.

MF1: Fine Mudstone.—Beds of fine mudstone with basal laminae (Fig. 7) are interpreted as fine-grained densites. MF1a represents waning flows that eroded the substrate to produce basal scours and subsequently deposited basal laminae, cross-laminae, and graded or structureless fine mud. As the sharp basal surfaces of MF1a reflect erosion, they are bedding planes that separate very thin beds (Fig. 7E). The scours and silt laminae of MF1a resemble those from other studies that are associated with bedload transport of mud (Schieber et al. 2007; Schieber and Southard 2009; Yawar and Schieber 2017).

In contrast to MF1a, laminae in MF1b (fine mudstone with parallel laminae; Fig. 8) are not associated with scours. Therefore, the mud that forms MF1b is interpreted to have settled from suspension.

The burrowed fine mudstone (MF1c; Fig. 9) may reflect a variety of processes that, due to burrowing, are difficult to reconstruct. Some of the burrowed fine mudstones bear calcispheres (Fig. 9), however, which indicates deposition by settling from suspension through the water column (see MF4: calcisphere packstone). There are also indications that some beds of MF1c are the product of more dynamic processes, such as sediment gravity flows: The burrowed fine mudstones often contain the

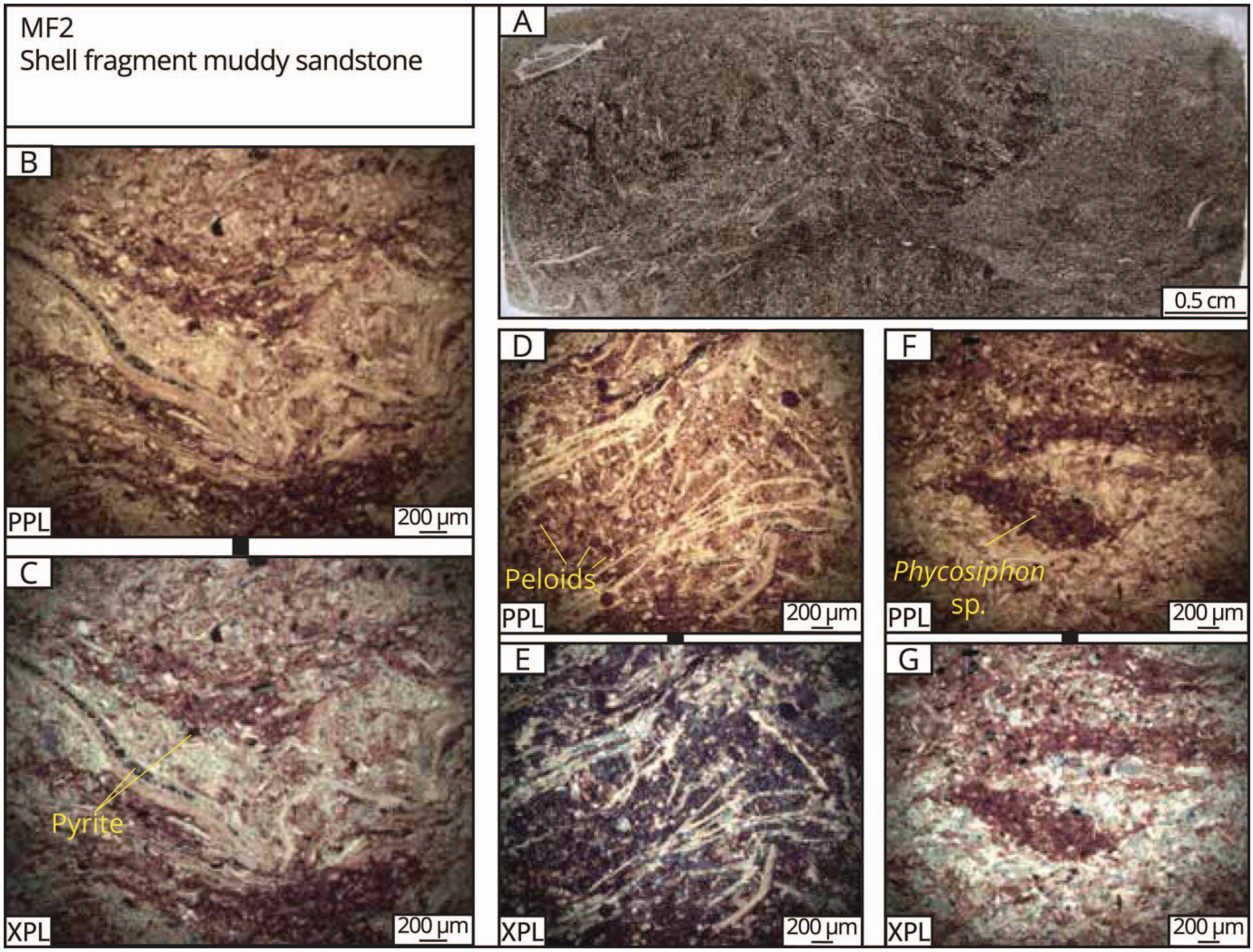

FIG. 10.—MF2: shell-fragment muddy sandstone, interpreted to represent reworked deposits. **A)** Thin-section overview showing fine shell fragments in most of the fabric, with subordinate coarser shell fragments and mud-filled burrows. **B**, **C)** The shell fragments are cemented together and sometimes filled in with pyrite. **D**, **E)** Sample that shows calcareous shell fragments in a siliceous matrix. **F**, **G)** The characteristic fishhook shape of *Phycosiphon* sp., which is often associated with event deposition (e.g., Rodríguez-Tovar et al. 2014).

trace fossil *Phycosiphon* sp. (Fig. 9B), which has been linked to early colonization following rapid sedimentation events (e.g., Rodríguez-Tovar et al. 2014). The sand-size peloids, preserved in carbonate concretions of several fine mudstones (Fig. 8B), suggest that the primary texture of the mud was peloidal. Peloids can be transported as bedload (Schieber et al. 2013; Birgenheier and Moore 2018). Some of the fine mud is associated with outsized clasts, such as shell fragments and plant material in FA2 (see Witmer 2007). In summary, the burrowed fine mudstones of the McCarthy Formation may represent background sedimentation but also more dynamic processes.

MF2: Shell-Fragment Muddy Sandstone.—Fragmented shallow-water bioclasts suggest that beds of this microfacies (Fig. 10) represent reworked deposits. The high intensity of bioturbation makes it difficult to recognize sedimentary structures, and thus the depositional processes behind the reworking and deposition of shallow-water bioclasts in deeper water are unclear. The deposition of beds of this microfacies likely occurred episodically, as the presence of *Phycosiphon* sp. (Fig. 10F) is often associated with event deposits (e.g., Rodríguez-Tovar et al. 2014).

MF3: Glauconitic Sandstone.—Glauconitic sandstones (Fig. 11) represent multiple depositional processes in a chemical environment that was suitable for *in situ* glauconitization. Since glauconitization is observed in both reworked and pelagic clasts, we interpret it as having occurred *in situ*. The uniform size and well-rounded shape of the glauconite grains indicate that the majority are glauconitized fecal pellets. Fecal pellets can form *in situ* but can also be transported over long distances (Schieber 2016), and the association of these pellets with reworked clasts, such as shell fragments (Fig. 11B), suggests that the fecal pellets underwent transport. Alternatively, the grains may represent abraded micritized skeletal grains. Other grains include foraminiferal tests (Fig. 11F) and fossils of *Heterastridium*, a hydrozoan with a planktic lifestyle (Schäfer and Grant-Mackie 1998).

MF4: Calcisphere Packstone.—Beds of this microfacies (Fig. 13) are the product of settling from suspension of pelagic skeletal material. Calcisphere packstones have often been interpreted as deposits of blooms that produce pelagic event beds (e.g., Tew 2000; Wilkinson 2011; Omaña et al. 2014). We interpret blooms to have caused rapid, episodic deposition

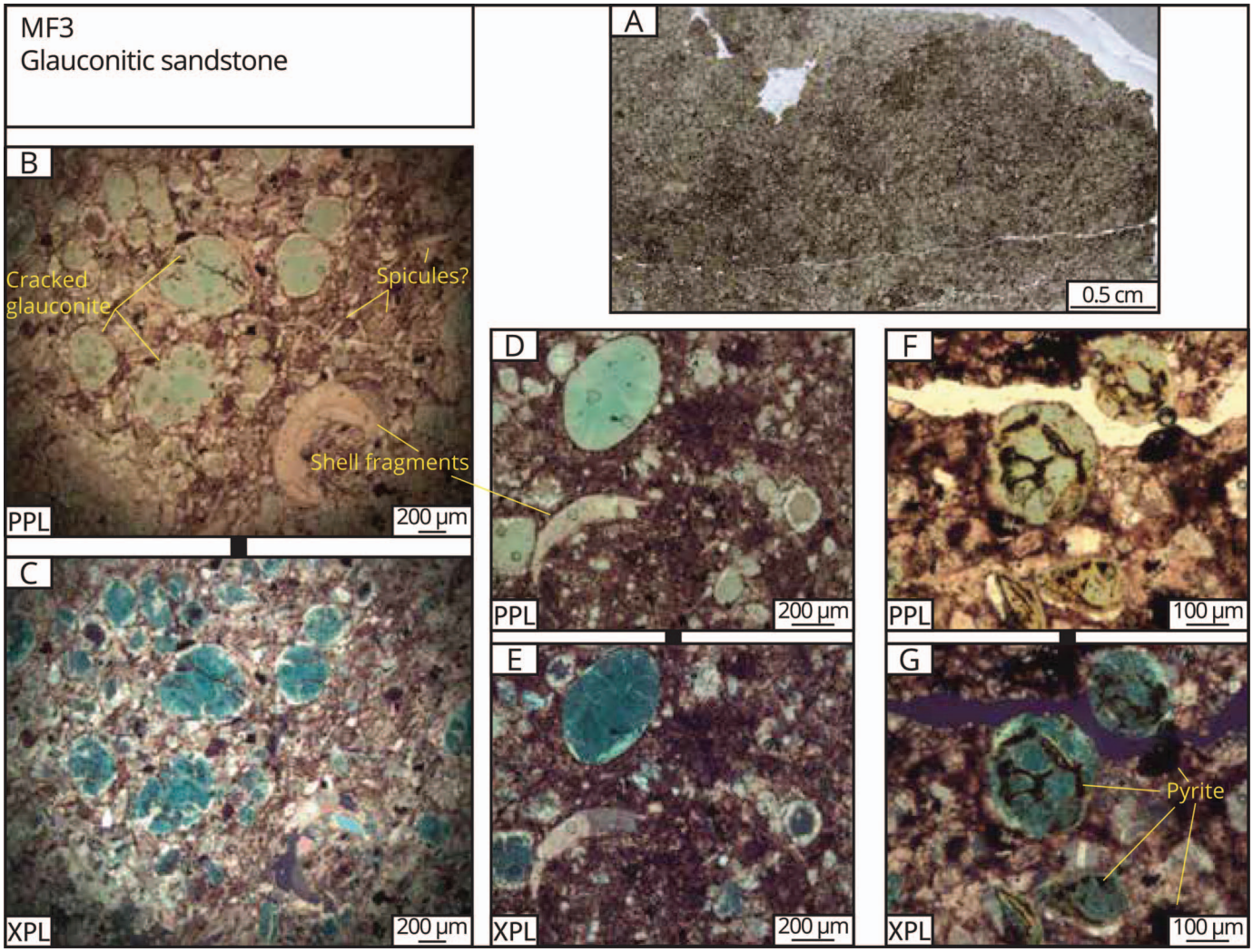

FIG. 11.—MF3: glauconitic muddy sandstone, interpreted to represent reworking followed by *in situ* glauconitization. **A)** Thin-section overview. **B**, **C)** The glauconite is associated with reworked shell fragments and subordinate spicules. **D**, **E)** The uniform, well-rounded glauconite grains are interpreted as glauconitized fecal pellets. **F**, **G)** Some glauconite grains are glauconitized microfossils, evidenced by the internal, foraminiferal, structures of these grains.

of calcispheres, which outpaced the muddy background sedimentation to form packstones. The interpretation of episodic blooms is also supported by the presence of *Phycosiphon* sp. (Fig. 13).

MF5: Spiculitic Sandy Mudstone.—The relatively poorly sorted assemblage of broken bioclasts suggests that this microfacies is the product of reworking (Fig. 16). This microfacies occurs in cherts and carbonate concretionary horizons. These rocks have a similar spiculitic framework, but the concretions contain less mud and more sparite (Fig. 16C–F). We interpret the textural contrast between cherts and concretions as the result of winnowing, which removed the fine siliceous mud from the beds in which carbonate concretions would grow soon after, during early diagenesis.

MF6: Laminated Sandy Mudstone.—The medium to thick beds of MF6a show bigradational sorting—reverse to normal grading within the same bed (Fig. 17C)—and are therefore interpreted to represent bottom-current deposits (i.e., contourites). Whereas bigradational sorting is a diagnostic criterion for contourites (e.g., Stow and Faugères 2008; Rebesco et al. 2014; Rodríguez-Tovar et al. 2019), it has also been associated with hyperpycnal flows (e.g., Shanmugam 2018). In the McCarthy Formation, there is no evidence for fluvial influence on the depositional environment, so a contouritic origin seems likely. The basal, coarsening-upward laminaset and the small-scale cross-laminae in the lower part of beds (Fig. 18D–F) represent the waxing phase of the bottom current, whereas the planar laminae in the coarsest interval represent the peak flow velocity (Fig. 18A–C). The fining-upward laminaset represents the waning phase of the bottom current (Fig. 18A).

The wavy fabric that distinguishes MF6b (Fig. 18G) is interpreted to represent microbial mats (see Schieber 2007). Given the setting of the McCarthy Formation, below storm wave base, the organic filaments that sometimes drape the wavy laminae are interpreted as the lamellar remnants of aphotic microbial mats. Although this microfacies comprises biogenic fabrics, most of the fabric consists of detrital calcite grains, which, based on the association with MF6a, were probably deposited by bottom currents.

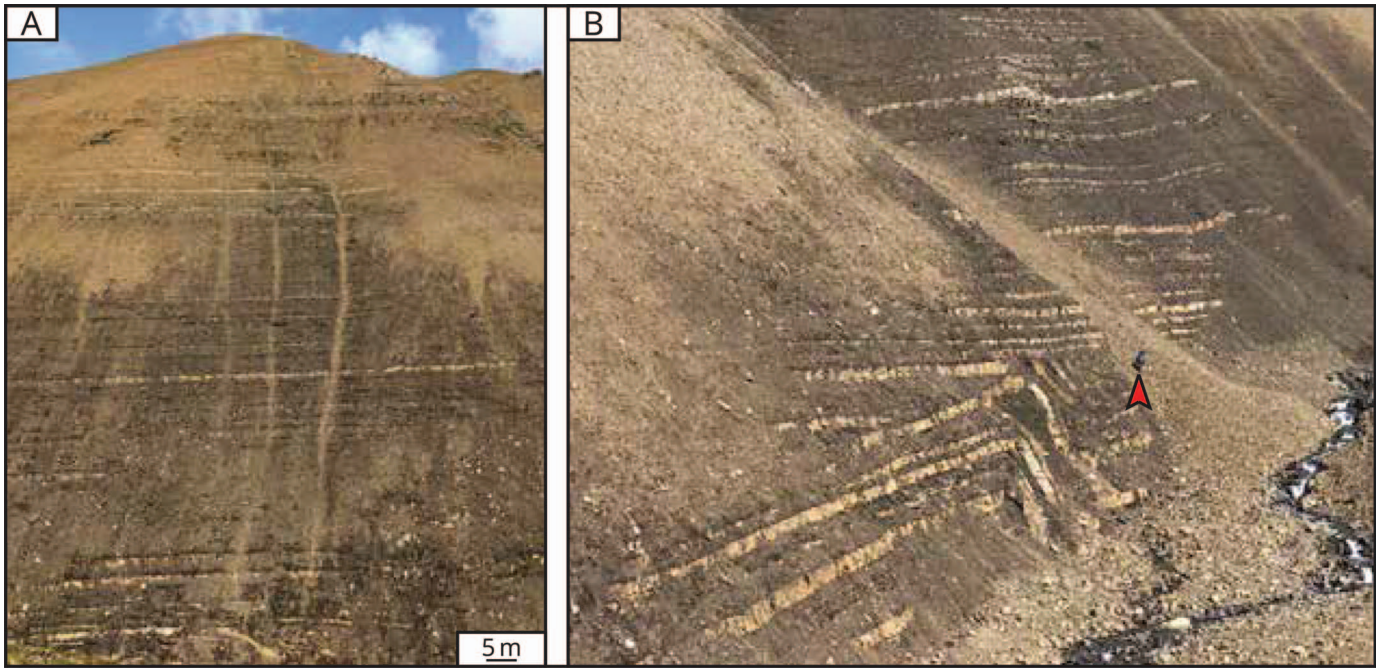

FIG. 12.—Facies association 2, interpreted as a sediment-starved outer-ramp environment on a siliceous carbonate-ramp. **A)** Photograph taken toward the west. FA2 is slope-forming and consists mostly of thin beds of burrowed fine mudstone (MF1c). The more prominent, thicker beds typically consist of calcisphere packstone (MF4). **B)** A syndepositional folding structure interpreted as a slump. Red arrow marks person for scale.

Sedimentology of the Outer McCarthy Ramp

Sediment Shedding to the Outer Ramp.—The absence of evidence for wave influence on the mudstones of the McCarthy Formation indicates that deposition took place below storm wave base. The depositional environment of the formation may, thus, be referred to as an outer ramp (*sensu* Burchette and Wright 1992).

We can infer that the outer ramp was a linear-sourced system (Reading and Richards 1994). The reworked bioclasts in MF2 and MF5 were produced in the biogenic sediment factory (e.g., Figs. 10, 16) which follows bathymetric contours and is therefore a linear sediment source. For this reason, the basin-scale architecture of the McCarthy Formation probably resembles that of linear-sourced siliciclastic slopes, in which lobes of reworked sediment are deposited everywhere, but not necessarily at the same time, along depositional strike (e.g., Surlyk 1987).

In the McCarthy Formation, reworked shallow-water sediment is concentrated stratigraphically in thick-bedded intervals (Figs. 6, 14), which are interpreted as lobe complexes (Fig. 19). Although most shallow-water grains are coarser skeletal grains (Figs. 10, 16), the lobe complex of FA1 also contains densitic mud (Fig. 7). Biogenic mud in ramps has been shown to be not only the product of background sedimentation but also to have been deposited by more dynamic processes (e.g., Schieber et al. 2013; Birgenheier and Moore 2018). In FA1 (Fig. 6), when shedding of calcareous skeletal grains and mud was not taking place, glauconitization took place (Fig. 11), nodules and concretions formed (e.g., Fig. 7A), and pelagic mud was deposited. The lobe complexes of FA1 and FA3 illustrate the impact of sediment gravity flows as a sediment delivery mechanism to the outer ramp, which is in line with previous studies that stress the role of reworking on ancient ramps (e.g., Puga-Bernabéu et al. 2014).

The alternation of thick-bedded (FA1 and FA3) and thin-bedded intervals (FA2 and FA4) represents fluctuating sediment supply to the outer ramp. The thick-bedded intervals represent lobe complexes, and the thin-bedded intervals were deposited when supply of shallow-water sediment to the outer ramp was reduced. The latter represent sediment-starved environments. This is evidenced by the relative scarcity of shallow-water skeletal grains, higher bioturbation indices (Figs. 9, 13), and low Rhaetian linear sedimentation rates (part of FA2) compared to the Hettangian (Table 2). Sediment-starved environments were dominated by background sedimentation, which is represented by burrowed fine mudstones (Fig. 9) and by calcisphere packstones, which represent pelagic blooms (Fig. 13). Though shedding of shallow-water skeletal grains was reduced, fine mud was still delivered to the outer ramp by turbidity currents. This behavior is similar to siliciclastic deepwater systems, where turbidity currents deliver mud to the basin floor when sand supply is reduced (Boulesteix et al. 2021).

Bottom Currents on the Outer Ramp.—The transition from MacKevett's (1963) lower (FA1 and FA2) to upper (FA3 and FA4) members reflects not only renewed sediment shedding to the outer ramp but also a change in the bottom-current regime: in the Hettangian, bottom currents started impacting deepwater sedimentation.

Few contourites have been identified in the Mesozoic so far (Creaser et al. 2017). The recognition of contourites in the rock record is still notoriously difficult, and even more so when the bottom current has modified a densite or turbidite (Stow and Smillie 2020), as is the case in the McCarthy Formation.

Bottom currents interact with topographic obstacles on the seafloor, such as oceanic plateaus, and this interaction deflects the currents and may increase their velocity (see Fig. 6a in Hernández-Molina et al. 2006, 2008). The increasing impact of bottom currents on the depositional environment of the McCarthy Formation may represent changing oceanographic conditions related to the tectonic journey of the seamount to higher latitudes or changes in oceanic circulation in Panthalassa related to climate change.

The sets of large-scale low-angle cross-stratification in FA3 (Fig. 15) are interpreted as a bottom current–induced sediment drift. FA3 contains channelforms (Fig. 15), dune cross-bedding (Fig. 14), and winnowed beds (Fig. 16C–F). In FA3, the textural contrast between carbonate concretions

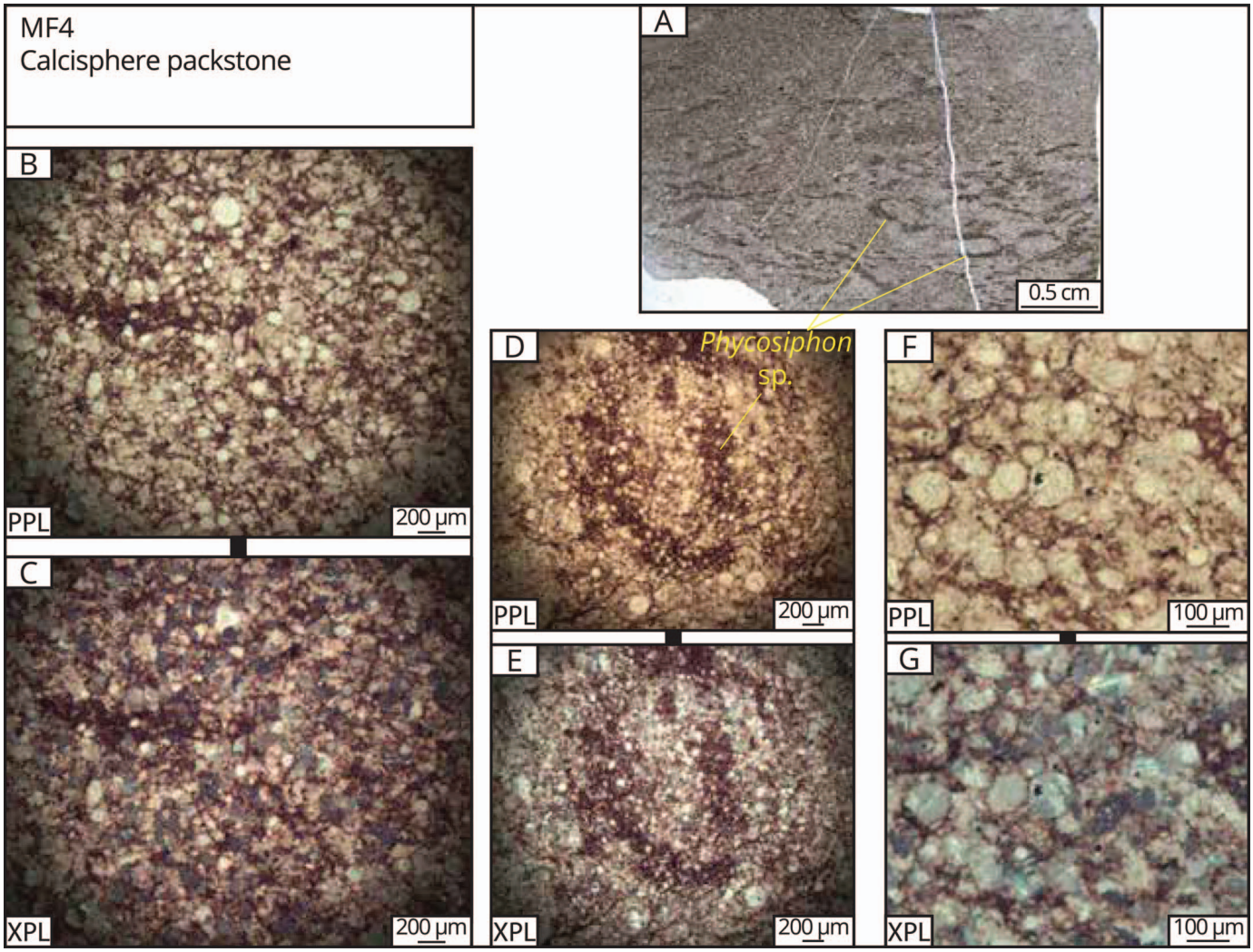

FIG. 13.—MF4: calcisphere packstone, interpreted to represent pelagic bloom deposits. **A)** Thin-section overview. The darker material represents mud-filled burrows. **B–G)** Outside the burrows, the fabric is rich in calcite cement. **D**, **E)** *Phycosiphon* sp. is associated with event deposition (e.g., Rodríguez-Tovar et al. 2014), which supports the interpretation of episodic blooms.

and cherts—both rich in siliceous spicules—is interpreted to be the product of winnowing by bottom currents: after muddy spiculitic sediment was shed to the outer ramp, bottom currents were strong enough to form subaqueous dunes of skeletal sand (Fig. 14) and to winnow siliceous mud from the strata in which carbonate concretions grew (Fig. 16C–F). Beds that were not affected by bottom currents contained enough siliceous mud to undergo chertification during burial (Fig. 16G).

Sets of large-scale cross-stratification in ramp records are often interpreted as progradational clinoforms on the slope of distally steepened ramps (e.g., Puga-Bernabéu et al. 2010, 2014), but compared to these examples, the sets of cross-stratification at Grotto Creek are smaller and less steep (Fig. 15). FA3 represents an outcrop analogue for biogenic drift systems that have been observed in seismic profiles (e.g., Reolid et al. 2019).

FA4 is not as well exposed as FA3, but sets of large-scale low-angle cross-stratification are not visible in the available outcrop (Fig. 17A). Nevertheless, FA4 is characterized by current-laminated fabrics and by bigradational beds (Fig. 17C), which we interpret as the product of bottom currents.

DISCUSSION

Rhaetian and Earliest Hettangian Sediment Starvation

The facies associations defined in this study represent changes in the composition and rate of biogenic sediment shedding from shallow water to the outer ramp. During deposition of FA2 (latest Norian Cordilleranus to earliest Hettangian Polymorphum zones; Caruthers et al. 2022), the outer ramp was sediment starved. Reduced biogenic sediment production rates on the ramp, combined with ongoing post-volcanic thermal subsidence (Trop et al. 2002), resulted in a long-term relative sea-level rise, a shutdown of sediment shedding to the basin, and sediment starvation on the outer ramp. This interval of sediment starvation lasted ~ 8.9 Myr (Fig. 4).

Sedimentation rates in the Rhaetian part of FA2 are much lower than in its Hettangian part, however (Table 2). Since there is no change in facies at the Triassic–Jurassic boundary, we conclude that the Rhaetian at Grotto Creek, though biostratigraphically complete (Caruthers et al. 2022), must contain several short hiatuses, without obvious unconformities, that explain lower sedimentation rates in the same facies. We infer that these Late Triassic hiatuses represent time intervals when the production of

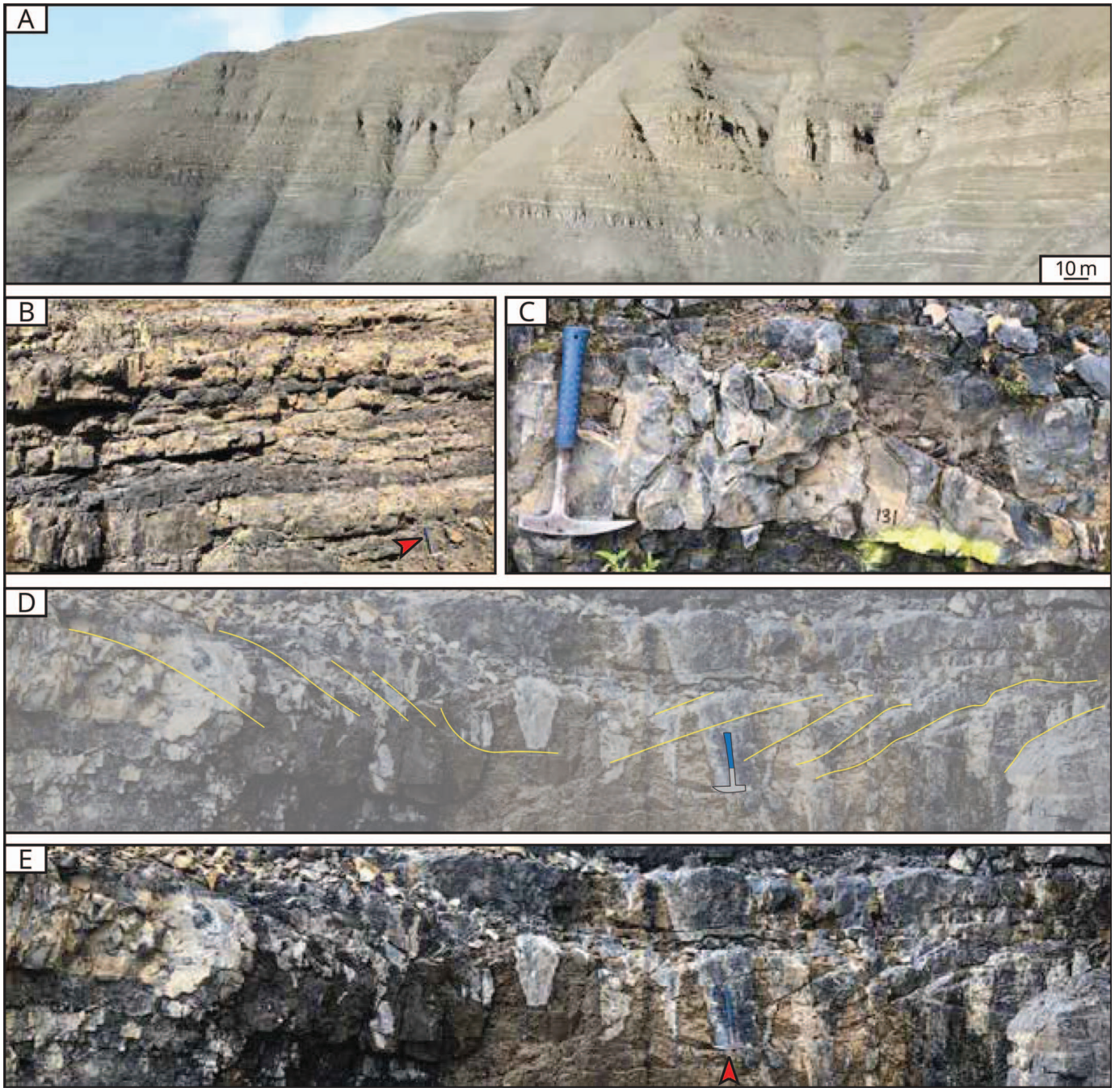

FIG. 14.—Facies association 3, interpreted as an outer-ramp lobe complex on a glass ramp. **A)** Photograph taken toward the west. **B)** FA3 consists of dark spiculitic chert and buff spiculitic concretionary horizons (both MF5). Red arrow marks hammer for scale. **C)** Sigmoidal cross-stratification that downlaps toward the right onto the bedding plane, interpreted as dune cross-stratification. **D**, **E)** Set of cross-stratification. Apparent dip directions are an artifact of the shape of the outcrop in the creek and represent dune migration directed away from the camera. Red arrow marks hammer for scale.

biogenic sediment either decreased or ceased. Calcisphere beds, which can be recognized throughout FA2 (Fig. 13), suggest that if carbonate dissolution occurred, it was not persistent but limited to several short phases.

Other Panthalassan records also suggest that sediment production rates may at times have been reduced due to the Late Triassic evolutionary turnover of radiolarians (e.g., Ward et al. 2001) and due to the impact of ocean acidification (e.g., Greene et al. 2012; Ikeda et al. 2015) and photic-zone euxinia (e.g., Kasprak et al. 2015; Fujisaki et al. 2018) on shallow-water carbonate producers.

Eustatic sea-level fluctuations had a minimal impact on the depositional environment of FA2. A long-term relative sea-level rise, resulting from post-volcanic subsidence, contributed to the shutdown of sediment shedding during the deposition of FA2 but no major shorter-term sea-level fluctuations can be recognized within this interval. At the Triassic–Jurassic boundary, a "regressive–transgressive couplet"—a eustatic sea-

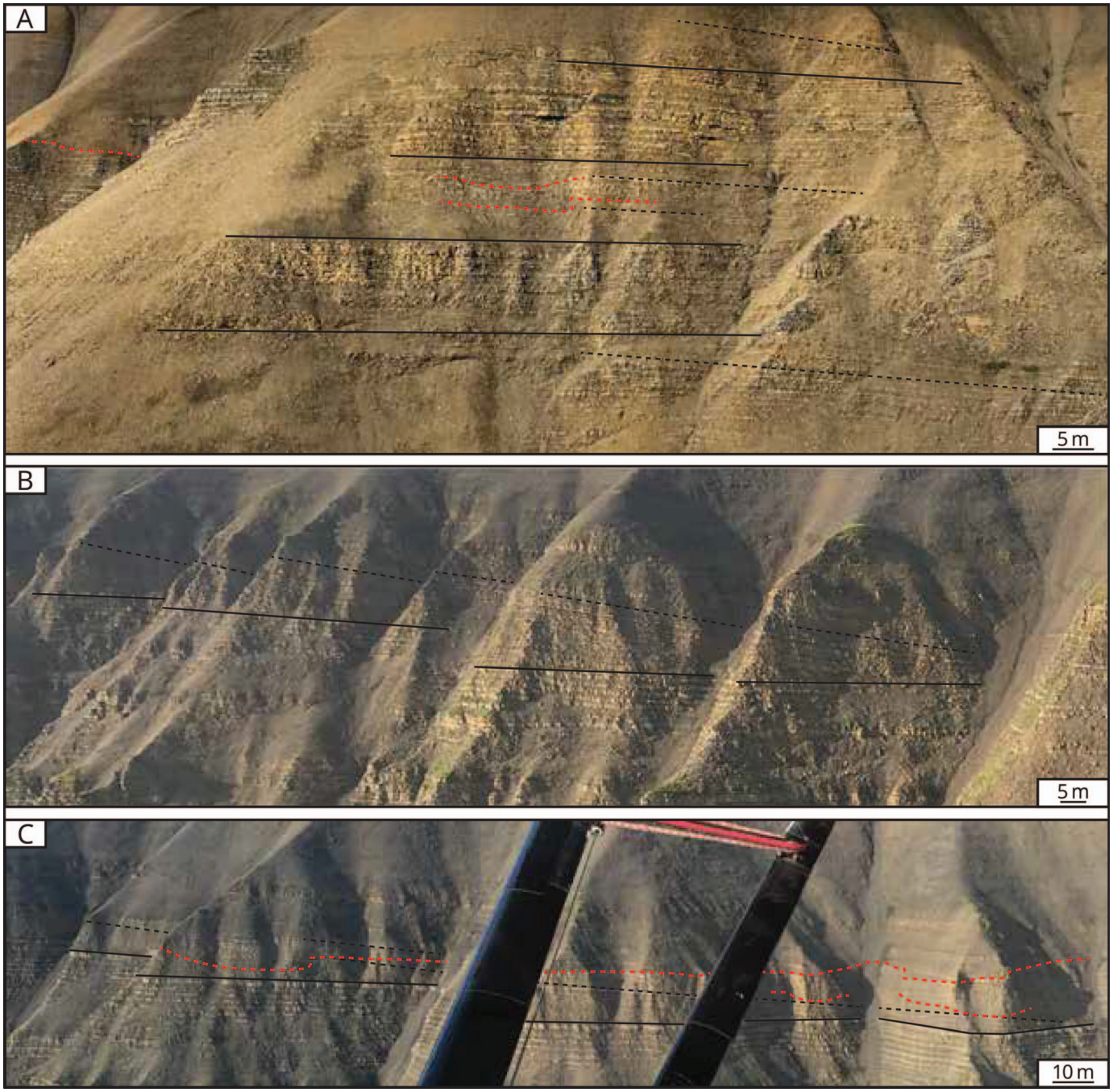

FIG. 15.—The large-scale architectural elements of FA3, interpreted as a bottom current-induced sediment drift. Continuous black lines mark planar-bedded stratification, dotted black lines mark low-angle cross-stratification, and the dotted red lines mark channelforms. The sets of cross-stratification have a height of 10–17 m and corrected dip angles of 6–8° (Heinhuis 2020). Part A was photographed toward the west in the Grotto Creek section. Parts B and C were photographed toward the southwest from an airplane about 2 km west of the Grotto Creek section.

level fall followed by a sharp rise—has been inferred (e.g., Hallam and Wignall 1999; Schoene et al. 2010). This sea-level record is found consistently across Europe (Hallam and Wignall 1999) and has also been recognized in a few Panthalassan sections (e.g., Wignall et al. 2007; Schoene et al. 2010; Peybernes et al. 2020). In the shallow-water sections of the Canadian continental margin, for example, the expression of the regressive phase is a major hiatus within the Rhaetian (Wignall et al. 2007). In deepwater environments, such as the outer McCarthy ramp, a sea-level fall should result in a basinward shift of facies and in the emplacement of a lowstand wedge, neither of which we observed in FA2.

The eustatic sea-level rise that is hypothesized to have followed the initial eustatic sea-level fall (Hallam and Wignall 1999; Schoene et al. 2010) should have resulted in a phase of condensation on the outer ramp in the earliest Hettangian. At Grotto Creek, however, the early Hettangian has a higher sedimentation rate than the Rhaetian. The lack of evidence for either a pronounced regressive or transgressive phase superposed on the longer-term transgression supports other studies that discount the eustatic

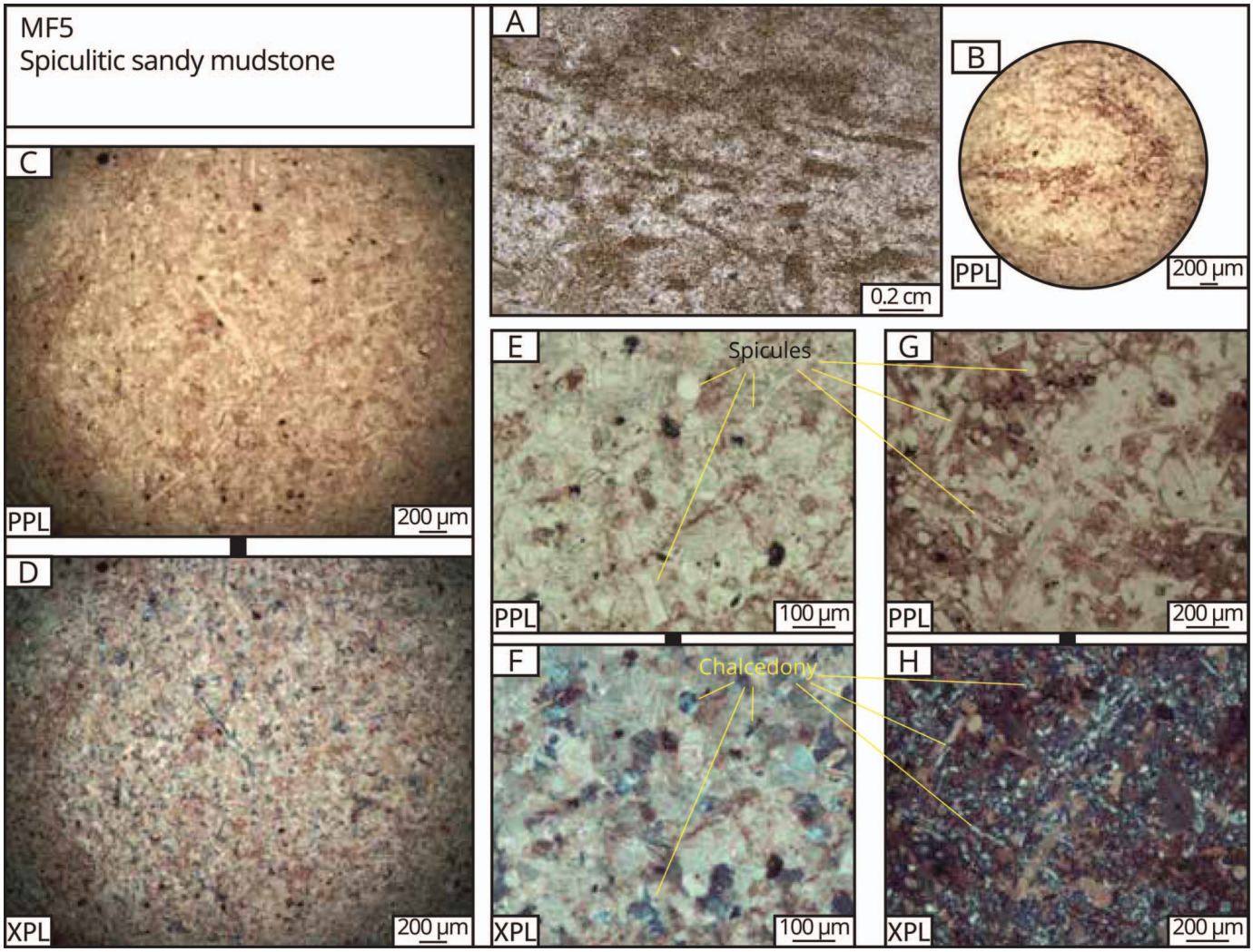

FIG. 16.—MF5: spiculitic sandy mudstone, interpreted to represent reworked deposits. This microfacies is present in the cherts and carbonate concretions of FA2. **A)** Thin-section overview of a spiculitic chert. **B)** *Phycosiphon* sp., which is associated with punctuated deposition (e.g., Rodríguez-Tovar et al. 2014). **C**–**F)** Concretions show siliceous spicules, which are filled with chalcedony, in sparry cement. **G**, **H)** Spiculitic chert. The concretions and the cherts both contain spicules, but the concretions contain less mud and more sparite than the cherts. This is interpreted to represent winnowing by bottom currents of the beds in which concretions would grow during early diagenesis.

nature of sea-level fluctuations at the Triassic–Jurassic boundary and their potential role as a global cause for mass extinction (e.g., Lucas and Tanner 2018).

Hettangian Recovery as a Glass Ramp

Following the mass-extinction interval, a recovery of the biogenic sediment factory is recorded in the McCarthy Formation at the boundary between the lower and upper members. This boundary marks a transition in the composition of shallow-water skeletal grains shed to the outer ramp from calcareous to siliceous. Thus, in the Hettangian, the depositional environment changed from a siliceous carbonate ramp to a glass ramp (Fig. 19).

The lower member represents the outer ramp of a siliceous carbonate ramp (Fig. 19). The facies that constitute the lower member are siliceous (Fig. 5A) and contain radiolarian tests, chert nodules, and microcrystalline silica (Fig. 5B). Most shallow-water skeletal grains in the lower member, however, are calcareous shell fragments, which form packstones (Fig. 10) or are incorporated in other facies (e.g., Fig. 11). Calcite-secreting organisms were the main contributors to sediment production in the shallow-water biogenic sediment factory during the Norian.

The glass-ramp environment of the upper member (Fig. 19) is reflected in the spiculitic microfacies (Fig. 16), which is similar to the transported spiculite facies of other Hettangian glass ramps (Ritterbush et al. 2014, 2016). The more siliceous nature of the upper member is also evidenced by bedded cherts, which are present only in the upper member (Fig. 5A), and by the quartz/calcite intensity ratios, which are generally higher in the upper member than in the lower member (Fig. S4). Although the upper member also contains minor calcareous skeletal grains and calcareous lithologies, most are concretions that, like most cherts, also contain spicules (Fig. 16C–F). The upper member therefore represents outer-ramp environments with a spiculitic sediment supply on a glass ramp, rather than deeper biofacies following a Hettangian eustatic deepening.

The transition from a siliceous carbonate ramp to a glass ramp recorded in the McCarthy Formation suggests that the biogeochemical regime that favored biosiliceous sedimentation was widespread in the Hettangian. The transition observed in this study is consistent with coeval records from the continental margins of Pangea (Delecat et al. 2011; Ritterbush et al. 2014, 2015, 2016). The presence of a glass ramp on Wrangellia, an isolated

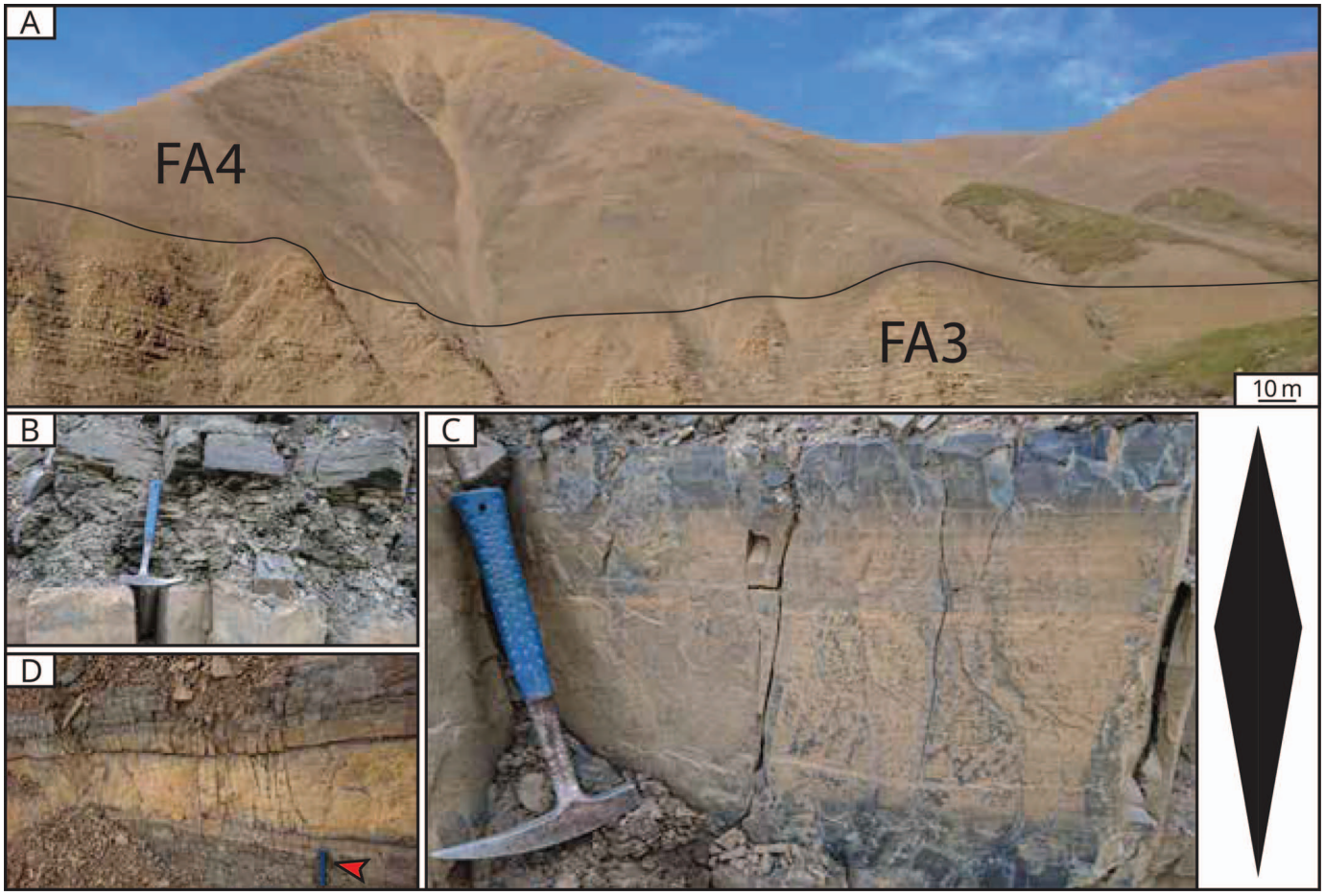

FIG. 17.—Facies association 4, interpreted as a sediment-starved outer-ramp environment on a glass ramp. **A)** Photograph taken toward the west. FA4 is slope-forming, although the upper half of FA4 also contains prominent beds. **B)** Most beds are thin and consist of burrowed fine mudstone (MF1c). **C)** Some of the thicker beds show bigradational sorting and are interpreted as contourites (MF6a). **D)** Some thicker beds are horizons of coalesced concretions, which can represent contourites (MF6a) and microbial mat colonization (MF6b).

oceanic plateau in the open Panthalassan Ocean (see also Jones et al. 1977; Trop et al. 2002), supports the hypothesis that weathering of CAMP basalts caused a global increase in oceanic silica concentrations, which promoted biosiliceous sedimentation and resulted in widespread glass ramps in the Early Jurassic (Ritterbush et al. 2015).

The transition to a glass ramp coincides with the base of the Mulleri Zone and occurred ~ 400 kyr after the Triassic–Jurassic boundary (Fig. 4). This timing is comparable to the ~ 600 kyr recovery reported in Peru and is consistent with the calculated timescale at which the weathering of CAMP basalts would have increased global oceanic silica concentrations (Ritterbush et al. 2015). This suggests that the increased silica supply on Wrangellia reflects a global signal rather than increased silica input from local Wrangellian basalts (i.e., the underlying Nikolai Greenstone). This is supported by the low Al%, which shows that total terrigenous sediment input to the ramp was low (Fig. 5A) and is consistent with the interpretation by Trop et al. (2002, p. 709) that there was "a general lack of high-relief, basin-bounding source terranes and volcanism" when the sediments of the McCarthy Formation were deposited.

The transition from a siliceous carbonate ramp to a glass ramp in the Hettangian coincided with an order-of-magnitude increase in linear sedimentation rates from FA2 to FA3 (Table 2). The low Rhaetian linear sedimentation rates represent a shutdown of sediment shedding and several short phases of stratigraphic condensation during and immediately after the end-Triassic mass extinction, whereas the higher Hettangian sedimentation rates represent the reactivation of the outer-ramp lobe complex as a result of increased sediment production during a proliferation of silica-secreting biota. This contrast illustrates the role of sediment production in the shallows in controlling the rate and the composition of the sediment supply to the outer ramp.

CONCLUSIONS

The McCarthy Formation represents Late Triassic to Early Jurassic biosiliceous sedimentation on a tropical outer ramp on Wrangellia.

- The ramp had a depositional dip toward the southwest.
- In both members of the McCarthy Formation, reworked sediment is concentrated in stratigraphic intervals that are interpreted as outer-ramp lobe complexes. The strata outside of lobe complexes represent sediment-starved outer-ramp environments where background sedimentation dominated.
- The sediment-starved interval in the Rhaetian and earliest Hettangian represents the end-Triassic mass extinction and its aftermath during which sediment shedding from the shallow ramp was inactive and pelagic sedimentation dominated.

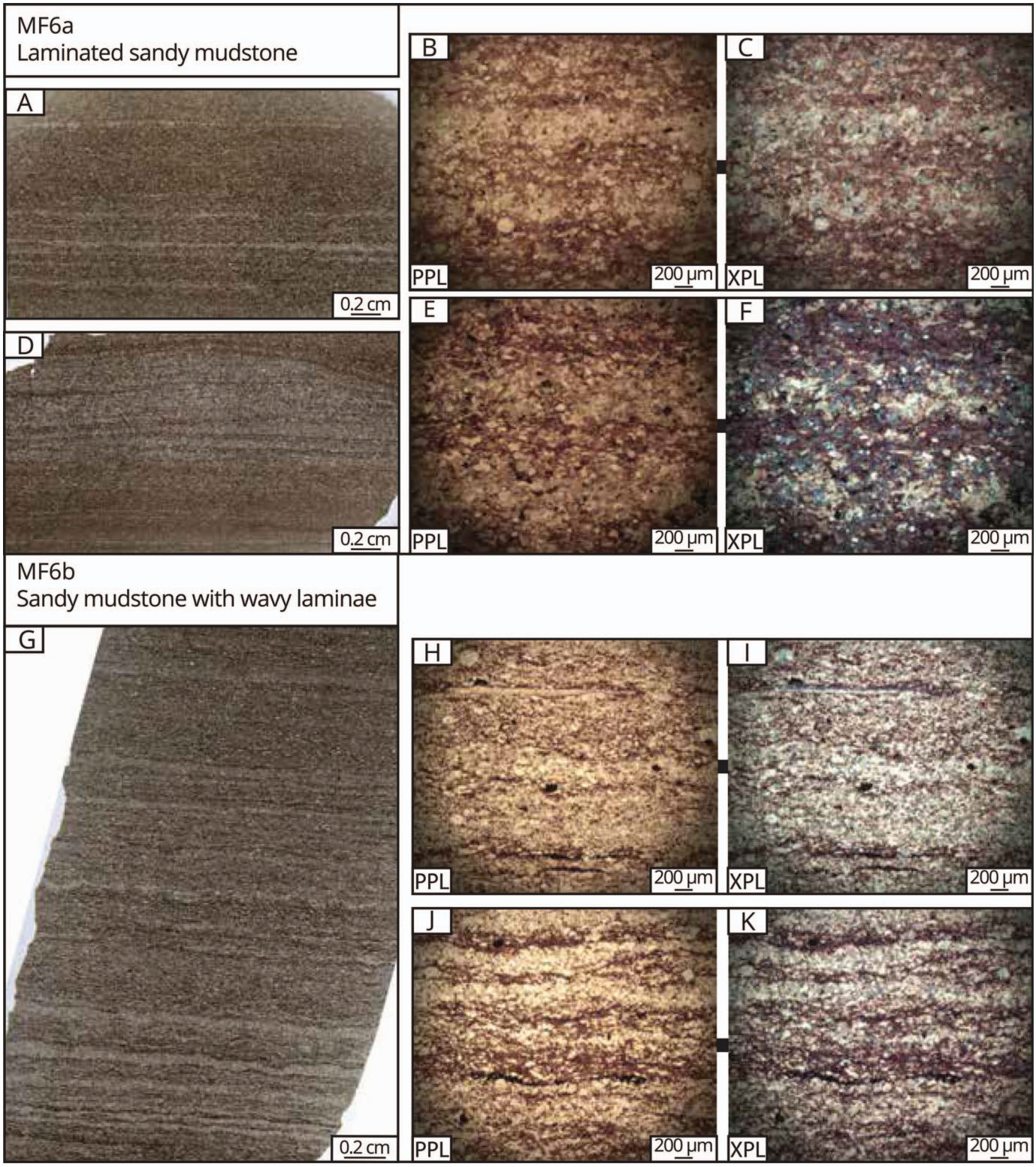

FIG. 18.—MF6: laminated sandy mudstone. **A–F)** MF6a is characterized by more planar laminae compared to MF6b and occurs in beds with bigradational sorting, which are interpreted as contourites. **A–C)** In thin section, the coarsest middle part of such beds contains planar-parallel laminae representing peak flow velocity. **D–F)** The finer material at the base of the bigradational beds contains slightly more siliceous fine mud, as well as basal and cross-laminae. **G–K)** MF6b is characterized by wavy laminae and represents a detrital deposit that was colonized by microbial mats. The laminae are sometimes draped by lamellar organic material (opaque).

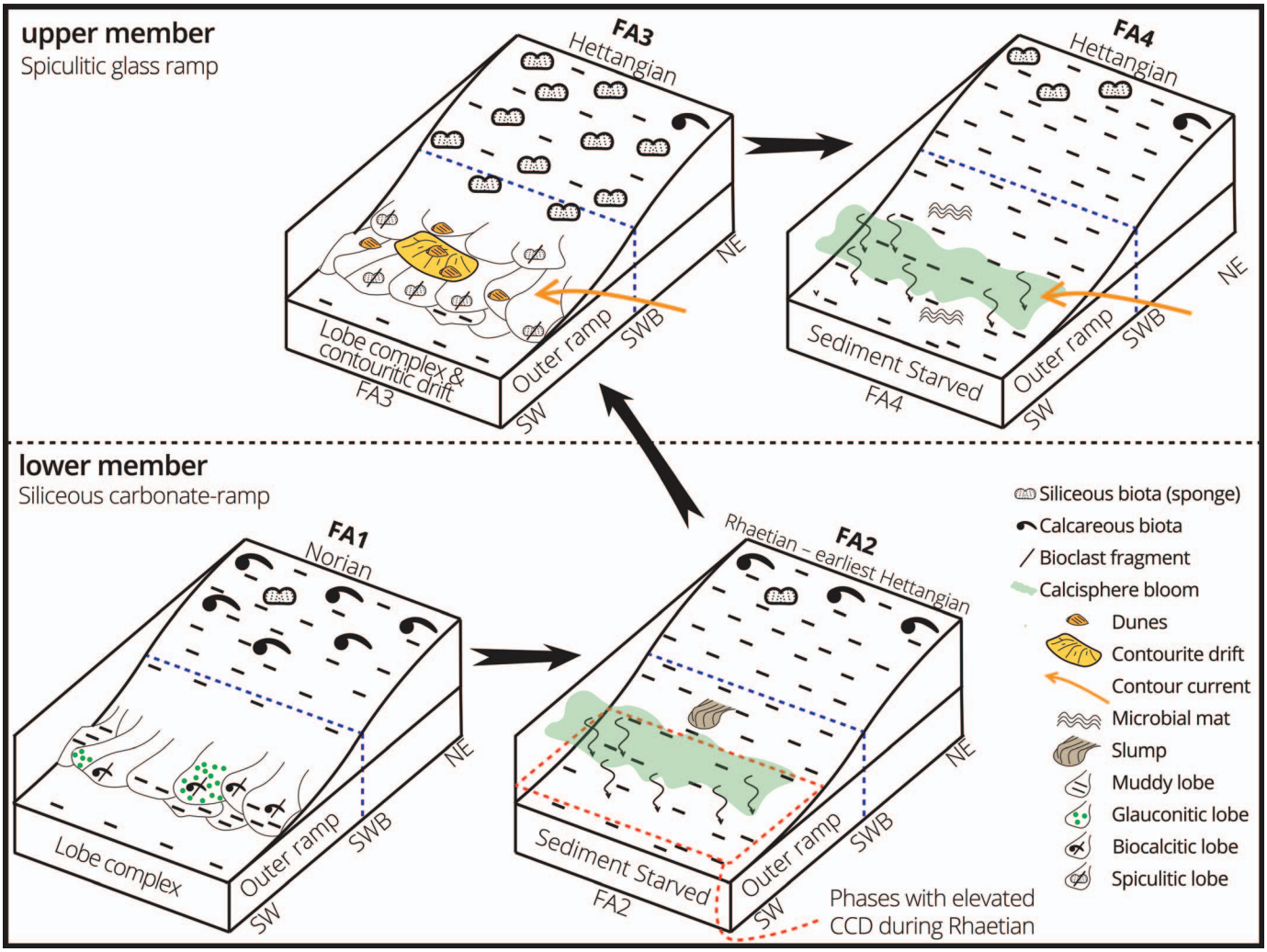

FIG. 19.—Schematic summary of the depositional environments of the McCarthy Formation. No scale is intended. The McCarthy Formation represents an outer ramp with a fluctuating supply of reworked shallow-water sediment, marked by the alternation of lobe complexes (FA1 and FA3) and sediment-starved environments (FA2 and FA4). During the deposition of the upper member, bottom currents affected deposition on the outer ramp. The member boundary marks a transition from a siliceous carbonate ramp to a spiculitic glass ramp in the Hettangian. This transition coincides with an order-of-magnitude increase in sedimentation rates, which illustrates how increased shallow-water sediment production can increase the sediment supply to the outer ramp. SWB, storm wave base.

- The Rhaetian is characterized by low sedimentation rates and stratigraphic condensation, which we infer is concentrated in several short hiatuses.
- During the Norian and Rhaetian, the lower member was deposited in the outer-ramp environments of a siliceous carbonate ramp. From Hettangian onwards, the upper member was deposited in the outer-ramp environments of a spiculitic glass ramp. This evolution represents a recovery phase of silica-secreting biota on Wrangellia following the end-Triassic mass extinction. This is consistent with coeval records from Pangea and supports the hypothesis that weathering of the Central Atlantic Magmatic Province increased global oceanic silica concentrations (e.g., Ritterbush et al. 2015; Ritterbush 2019).
- The member boundary represents the reactivation of sediment shedding and the onset of bottom current activity. Bottom currents resulted in a sediment drift on the outer ramp during the Hettangian.
- An order-of-magnitude increase in sedimentation rates at Grotto Creek from the Rhaetian to the Hettangian coincided with the transition from a siliceous carbonate ramp to a glass ramp, the reactivation of sediment shedding, and the onset of bottom-current activity.

SUPPLEMENTAL MATERIAL

Supplemental material is available from the SEPM Data Archive: https://www.sepm.org/supplemental-materials.

ACKNOWLEDGMENTS

We thank Mark Miller and Morgan Gantz at the Wrangell–St. Elias National Park and Preserve (research and collecting permit numbers WRST-2017-SCI-0004 and WRST-2018-SC1-0005), Paul and Jay Claus at Ultima Thule Lodge, and Anita van Leeuwen-Tolboom and Coen Mulder at Utrecht University. We thank Lauren Birgenheier and Kathleen Ritterbush for reviewing this manuscript. JPTA and YPV thank the Molengraaff Fund and SEPM for financial support of the fieldwork. Fieldwork was supported by a grant from the National Geographic Society (NGS-9973-16) to AHC. Analytical work by KM was supported by a grant from the National Science Foundation (EAR-2026926) to AHC, JDO, and BCG. Any opinions, findings, and conclusions or recommendations expressed in this material are those of the author(s) and do not necessarily reflect the views of the National Science Foundation.

TABLE 3.—*Descriptions of the microfacies of the McCarthy Formation (see also supplementary materials). BI, bioturbation index (Droser and Bottjer 1986).*

Microfacies	Subdivision	Code	Occurrence	Textures	Field Lithofacies	Sedimentary Structures	BI	Interpretation
Fine mudstone Dunham: mudstone–wackestone	With basal laminae	**MF1a** N = 6 Fig. 7	FA1; subordinate in FA2, FA3	Dominated by fine mud (~ 70–95%). Coarser grains are coarse mud to medium-sand-size grains of subangular quartz and calcite. Some sand grains are recognizable as radiolarians, calcispheres, or foraminifera. A few samples contain carbonate concretions that are rich in sand-size peloids. In the upper member, this microfacies is richer in chalcedony and siliceous bioclasts than in the lower member.	Medium gray to black siliceous mudstones and calcareous cherts, some of which are very thin to thin bedded, forming thin to medium bedsets, whereas others are medium to thick bedded. Beds of this microfacies are sometimes laminated.	Very thin continuous and discontinuous basal laminae and asymptotic cross-laminae. Grading.	2	Deposition by turbidity currents
	With parallel laminae	**MF1b** N = 3 Fig. 8	FA2; subordinate in FA1			Very thin to thin parallel laminae without basal scours.	2	Settling from suspension from water column
	Burrowed	**MF1c** N = 17 Fig. 9	Everywhere; most common in FA2, FA4			—	5–6	Settling from suspension; turbidity currents
Shell fragment muddy sandstone Dunham: packstone		**MF2** N = 2 Fig. 10	FA1	Rich in thin calcareous shell fragments (50–60%). The rest of the fabric consists of fine mud and coarse-mud-size calcite grains and peloids. Contains a few bryozoans.	Thin to thick beds of gray indurated sandy limestones.	—	4	Reworking
Glauconitic muddy sandstone Dunham: packstone–wackestone		**MF3** N = 3 Fig. 11	FA1	Characterized by well-rounded fine to medium glauconitic sand. The grains are glauconitized fecal pellets and microfossils. Bears fine mud, shell fragments, and coarse mud to sand-size grains of subangular calcite and contains few spicules.	Dark, medium to thick beds of glauconitic sandstone. One bed is a glauconitized packstone of *Heterastridium*.	—	5	Reworking, *in situ* glauconitization
Calcisphere packstone Dunham: packstone		**MF4** N = 9 Fig. 13	FA2; subordinate in FA1, FA3, FA4	Characterized by coarse mud and sand fractions (70–90%) that are dominated by calcispheres. Well-cemented and bears fine mud. Some samples contain a few spicules (< 5%).	Thin to thick beds of sandy limestone and calcareous chert. Often indurated and concretionary.	—	5	Settling from suspension from pelagic blooms
Spiculitic sandy mudstone Dunham: packstone		**MF5** N = 21 Fig. 16	FA3	Characterized by coarse mud and sand fractions (> 70%) rich in siliceous spicules. This microfacies occurs in cherts (more siliceous mud) and concretions (more sparite). Also contains echinoid fragments, radiolarians, calcispheres, and foraminifera.	Medium to thick beds of dark chert and buff-colored concretionary horizons.	Some concretionary beds contain cross bedding.	5	Reworking, winnowing by bottom currents

TABLE 3.—*Continued.*

Microfacies	Subdivision	Code	Occurrence	Textures	Field Lithofacies	Sedimentary Structures	BI	Interpretation
Laminated sandy mudstone Dunham: packstone	With planar laminae	**MF6a** N = 2 Fig. 18	FA4	Characterized by coarse mud and sand fractions (> 68%) of subangular calcite. These coarser grains are concentrated in well-cemented laminae. Contains calcispheres. Bears shell fragments and organic material.	Medium to thick buff-colored beds of calcareous chert. Sometimes concretionary.	Bigradational sorting within beds. In thin section, the coarsest parts of such beds contain very thin planar parallel laminae. Finer parts contain basal fining-upward laminae and sigmoidal cross-laminae.	1	Reworking by bottom currents
	With wavy laminae	**MF6b** N = 3 Fig. 18	FA4			Very thin wavy laminae that are sometimes draped by organic material.	1	Microbial-mat colonization

REFERENCES

ARMSTRONG, A.K., MACKEVETT, E.M., AND SILBERLING, N.J., 1969, The Chitistone and Nizina limestones of part of the southern Wrangell Mountains, Alaska: a preliminary report stressing carbonate petrography and depositional environments: U.S. Geological Survey, Professional Paper 650-D, p. 49–62.

BACCELLE, L., AND BOSELLINI, A., 1965, Diagrammi per la stima visiva della composizione percentuale nelle rocce sedimentarie: Università di Ferrara, Annali (Nuova Serie). Sezione IX Scienze Geologiche e Paleontologiche, v. 1, p. 59–62.

BIRGENHEIER, L.P., AND MOORE, S.A., 2018, Carbonate mud deposited below storm wave base: a critical review: The Sedimentary Record, v. 16, p. 4–10, doi:10.2110/sedred.2018.4.4.

BLACKBURN, T.J., OLSEN, P.E., BOWRING, S.A., MCLEAN, N.M., KENT, D.V., PUFFER, J., MCHONE, G., RASBURY, E.T., AND ET-TOUHAMI, M., 2013, Zircon U-Pb Geochronology links the end-Triassic extinction with the Central Atlantic Magmatic Province: Science, v. 340, p. 941–945, doi:10.1126/science.1234204.

BOULESTEIX, K., POYATOS-MORÉ, M., HODGSON, D.M., FLINT, S.S., AND TAYLOR, K.G., 2021, Fringe or background: characterizing deep-water mudstones beyond the basin-floor fan sandstone pinchout: Journal of Sedimentary Research, v. 90, p. 1678–1705, doi:10.2110/jsr.2020.048.

BURCHETTE, T.P., AND WRIGHT, V.P., 1992, Carbonate ramp depositional systems: Sedimentary Geology, v. 79, p. 3–57, doi:10.1016/0037-0738(92)90003-A.

BUTLER, R.F., GEHRELS, G.E., AND BAZARD, D.R., 1997, Paleomagnetism of Paleozoic strata of the Alexander terrane, southeastern Alaska: Geological Society of America, Bulletin, v. 109, p. 1372–1388, doi:10.1130/0016-7606(1997)109<1372:POPSOT>2.3.CO;2.

CAMPBELL, C.V., 1967, Lamina, laminaset, bed and bedset: Sedimentology, v. 8, p. 7–26, doi:10.1111/j.1365-3091.1967.tb01301.x.

CARUTHERS, A.H., AND STANLEY, G.D., 2008, Late Triassic silicified shallow-water corals and other marine fossils from Wrangellia and the Alexander terrane, Alaska, and Vancouver Island, British Columbia, *in* Blodgett, R.B., and Stanley, G.D., Jr., eds., The Terrane Puzzle: New Perspectives on Paleontology and Stratigraphy from the North American Cordillera: Geological Society of America, Special Papers, v. 442, p. 151–179, doi:10.1130/2008.442(10).

CARUTHERS, A.H., MARROQUÍN, S.M., GRÖCKE, D.R., GOLDING, M.L., ABERHAN, M., THEM, T.R., VEENMA, Y.P., OWENS, J.D., MCROBERTS, C.A., FRIEDMAN, R.M., TROP, J.M., SZŰCS, D., PÁLFY, J., RIOUX, M., TRABUCHO-ALEXANDRE, J.P., AND GILL, B.C., 2022, New evidence for a long Rhaetian from a Panthalassan succession (Wrangell Mountains, Alaska) and regional differences in carbon cycle perturbations at the Triassic–Jurassic transition: Earth and Planetary Science Letters, v. 577, no. 117262, doi:10.1016/j.epsl.2021.117262.

CREASER, A., HERNÁNDEZ-MOLINA, F.J., BADALINI, G., THOMPSON, P., WALKER, R., SOTO, M., AND CONTI, B., 2017, A Late Cretaceous mixed (turbidite–contourite) system along the Uruguayan Margin: sedimentary and palaeoceanographic implications: Marine Geology, v. 390, p. 234–253, doi:10.1016/j.margeo.2017.07.004.

ČRNE, A.E., WEISSERT, H., GORIČAN, Š., AND BERNASCONI, S.M., 2011, A biocalcification crisis at the Triassic–Jurassic boundary recorded in the Budva Basin (Dinarides, Montenegro): Geological Society of America, Bulletin, v. 123, p. 40–50, doi:10.1130/B30157.1.

CSEJTEY, B., COX, D.P., EVARTS, R.C., STRICKER, G.D., AND FOSTER, H.L., 1982, The Cenozoic Denali fault system and the Cretaceous accretionary development of southern Alaska: Journal of Geophysical Research: Solid Earth, v. 87, p. 3741–3754, doi:10.1029/JB087iB05p03741.

DELECAT, S., ARP, G., AND REITNER, J., 2011, Aftermath of the Triassic–Jurassic boundary crisis: spiculite formation on drowned Triassic Steinplatte reef-slope by communities of Hexactinellid sponges (Northern Calcareous Alps, Austria), *in* Reitner, J., Quéric, N.-V., and Arp, G., eds., Advances in Stromatolite Geobiology: Berlin, Springer, Lecture Notes in Earth Sciences, v. 131, p. 355–390, doi:10.1007/978-3-642-10415-2_23.

DROSER, M.L., AND BOTTJER, D.J., 1986, A semiquantitative field classification of ichnofabric: Journal of Sedimentary Petrology, v. 56, p. 558–559, doi:10.1306/212F89C2-2B24-11D7-8648000102C1865D.

DUNHAM, R.J., 1962, Classification of carbonate rocks according to depositional textures, *in* Ham, W.E., ed., Classification of Carbonate Rocks: A Symposium: American Association of Petroleum Geologists, Memoir, v. 1, p. 108–121.

FUJISAKI, W., MATSUI, Y., ASANUMA, H., SAWAKI, Y., SUZUKI, K., AND MARUYAMA, S., 2018, Global perturbations of carbon cycle during the Triassic–Jurassic transition recorded in the mid-Panthalassa: Earth and Planetary Science Letters, v. 500, p. 105–116, doi:10.1016/j.epsl.2018.07.026.

GALLI, M.T., JADOUL, F., BERNASCONI, S.M., AND WEISSERT, H., 2005, Anomalies in global carbon cycling and extinction at the Triassic–Jurassic boundary: evidence from a marine C-isotope record: Palaeogeography, Palaeoclimatology, Palaeoecology, v. 216, p. 203–214, doi:10.1016/j.palaeo.2004.11.009.

GATES, L.M., JAMES, N.P., AND BEAUCHAMP, B., 2004, A glass ramp: shallow-water Permian spiculitic chert sedimentation, Sverdrup Basin, Arctic Canada: Sedimentary Geology, v. 168, p. 125–147, doi:10.1016/j.sedgeo.2004.03.008.

GREENE, A.R., SCOATES, J.S., WEIS, D., KATVALA, E.C., ISRAEL, S., AND NIXON, G.T., 2010, The architecture of oceanic plateaus revealed by the volcanic stratigraphy of the accreted Wrangellia oceanic plateau: Geosphere, v. 6, p. 47–73, doi:10.1130/GES00212.1.

GREENE, S.E., MARTINDALE, R.C., RITTERBUSH, K.A., BOTTJER, D.J., CORSETTI, F.A., AND BERELSON, W.M., 2012, Recognising ocean acidification in deep time: an evaluation of

the evidence for acidification across the Triassic–Jurassic boundary: Earth-Science Reviews, v. 113, p. 72–93, doi:10.1016/j.earscirev.2012.03.009.

Hallam, A., and Wignall, P.B., 1999, Mass extinctions and sea-level changes: Earth-Science Reviews, v. 48, p. 217–250.

Heinhuis, Y., 2020, Architecture of a glass ramp: the McCarthy Formation, southcentral Alaska [BA Thesis]: Universiteit Utrecht, 38 p.

Hernández-Molina, F.J., Larter, R.D., Rebesco, M., and Maldonado, A., 2006, Miocene reversal of bottom water flow along the Pacific Margin of the Antarctic Peninsula: stratigraphic evidence from a contourite sedimentary tail: Marine Geology, v. 228, p. 93–116, doi:10.1016/j.margeo.2005.12.010.

Hernández-Molina, F.J., Maldonado, A., and Stow, D.A.V., 2008, Abyssal plain contourites, *in* Rebesco, M., and Camerlenghi, A., eds., Contourites: Amsterdam, Elsevier, Developments in Sedimentology, v. 60, p. 345–378, doi:10.1016/S0070-4571(08)10018-8.

Hesselbo, S.P., Ogg, J.G., Ruhl, M., Hinnov, L.A., and Huang, C.J., 2020, The Jurassic Period, *in* Gradstein, F.M., Ogg, J.G., Schmitz, M.D., and Ogg, G.M., eds., Geologic Time Scale 2020: Amsterdam, Elsevier, p. 955–1021, doi:10.1016/B978-0-12-824360-2.00026-7.

Hillebrandt, A.V., Krystyn, L., Kürschner, W.M., Bonis, N.R., Ruhl, M., Richoz, S., Schobben, M.A.N., Urlichs, M., Bown, P.R., Kment, K., McRoberts, C.A., Simms, M., and Tomášových, A., 2013, The global stratotype sections and point (GSSP) for the base of the Jurassic System at Kuhjoch (Karwendel Mountains, Northern Calcareous Alps, Tyrol, Austria): Episodes, v. 36, p. 162–198, doi:10.18814/epiiugs/2013/v36i3/001.

Hillhouse, J.W., and Coe, R.S., 1994, Paleomagnetic data from Alaska, *in* Plafker, G., and Berg, H.C., eds., The Geology of Alaska: Geological Society of America, The Geology of North America v. G-1, p. 797–821, doi:10.1130/DNAG-GNA-G1.797.

Hillhouse, J.W., and Gromme, C.S., 1984, Northward displacement and accretion of Wrangellia: new paleomagnetic evidence from Alaska: Journal of Geophysical Research, Solid Earth, v. 89, p. 4461–4477, doi:10.1029/JB089iB06p04461.

Ikeda, M., Hori, R.S., Okada, Y., and Nakada, R., 2015, Volcanism and deep-ocean acidification across the end-Triassic extinction event: Palaeogeography, Palaeoclimatology, Palaeoecology, v. 440, p. 725–733, doi:10.1016/j.palaeo.2015.09.046.

Jones, D.L., and Murchey, B., 1986, Geologic significance of Paleozoic and Mesozoic radiolarian chert: Annual Review of Earth and Planetary Sciences, v. 14, p. 455–492.

Jones, D.L., Silberling, N.J., and Hillhouse, J., 1977, Wrangellia: a displaced terrane in northwestern North America: Canadian Journal of Earth Sciences, v. 14, p. 2565–2577, doi:10.1139/e77-222.

Kasprak, A.H., Sepúlveda, J., Price-Waldman, R., Williford, K.H., Schoepfer, S.D., Haggart, J.W., Ward, P.D., Summons, R.E., and Whiteside, J.H., 2015, Episodic photic zone euxinia in the northeastern Panthalassic Ocean during the end-Triassic extinction: Geology, v. 43, p. 307–310, doi:10.1130/G36371.1.

Korte, C., Ruhl, M., Pálfy, J., Ullmann, C.V., and Hesselbo, S.P., 2018, Chemostratigraphy across the Triassic–Jurassic Boundary, *in* Sial, A.N., Gaucher, C., Ramkumar, M., and Ferreira, PintoV., eds., Chemostratigraphy across Major Chronological Boundaries: American Geophysical Union, Geophysical Monograph, v. 240, p. 183–210, doi:10.1002/9781119382508.ch10.

Krencker, F.-N., Bodin, S., Suan, G., Heimhofer, U., Kabiri, L., and Immenhauser, A., 2015, Toarcian extreme warmth led to tropical cyclone intensification: Earth and Planetary Science Letters, v. 425, p. 120–130, doi:10.1016/j.epsl.2015.06.003.

Lazar, O.R., Bohacs, K.M., Macquaker, J.H.S., Schieber, J., and Demko, T.M., 2015, Capturing key attributes of fine-grained sedimentary rocks in outcrops, cores, and thin sections: nomenclature and description guidelines: Journal of Sedimentary Research, v. 85, p. 230–246, doi:10.2110/jsr.2015.11.

Lucas, S.G., and Tanner, L.H., 2018, The missing mass extinction at the Triassic–Jurassic Boundary, *in* Tanner, L.H., ed., The Late Triassic World: Earth in a Time of Transition: Cham, Springer, Topics in Geobiology, v. 46, p. 721–785, doi:10.1007/978-3-319-68009-5_15.

MacKevett, E.M., 1963, Preliminary geologic map of the McCarthy C-5 quadrangle, Alaska: U.S. Geological Survey, IMAP 406, doi:10.3133/i406.

MacKevett, E.M., 1969, Three newly named Jurassic formations in the McCarthy C-5 Quadrangle, Alaska: U.S. Geological Survey, Bulletin 1274-A, p. 35–49.

MacKevett, E.M., 1970a, Geologic map of the McCarthy C-4 quadrangle, Alaska: U.S. Geological Survey, Geologic Quadrangle 844, doi:10.3133/gq844.

MacKevett, E.M., 1970b, Geologic map of the McCarthy C-5 quadrangle, Alaska: U.S. Geological Survey, Geologic Quadrangle 899, doi:10.3133/gq899.

MacKevett, E.M., 1972, Geologic map of the McCarthy C-6 quadrangle, Alaska: U.S. Geological Survey, Geologic Quadrangle 979, doi:10.3133/gq979.

MacKevett, E.M., 1974, Geologic map of the McCarthy B-5 quadrangle, Alaska: U.S. Geological Survey, Geologic Quadrangle 1146, doi:10.3133/gq1146.

MacKevett, E.M., 1978, Geologic map of the McCarthy Quadrangle, Alaska: U.S. Geological Survey, IMAP 1032, doi:10.3133/i1032.

MacKevett, E.M., and Smith, J.G., 1972a, Geologic map of the McCarthy B-4 quadrangle, Alaska: U.S. Geological Survey, Geologic Quadrangle 943, doi:10.3133/gq943.

MacKevett, E.M., and Smith, J.G., 1972b, Geologic map of the McCarthy B-6 quadrangle, Alaska: U.S. Geological Survey, Geologic Quadrangle 1035, doi:10.3133/gq1035.

MacKevett, E.M., Smith, J.G., Jones, D.L., and Winkler, G.R., 1978, Geologic map of the McCarthy C-8 quadrangle, Alaska: U.S. Geological Survey, Geologic Quadrangle 1418, doi:10.3133/gq1418.

Macquaker, J.H.S., and Adams, A.E., 2003, Maximizing information from fine-grained sedimentary rocks: an inclusive nomenclature for mudstones: Journal of Sedimentary Research, v. 73, p. 735–744, doi:10.1306/012203730735.

Martin, G.C., 1916, Triassic rocks of Alaska: Geological Society of America, Bulletin, v. 27, p. 685–718, doi:10.1130/GSAB-27-685.

McCave, I.N., Manighetti, B., and Robinson, S.G., 1995, Sortable silt and fine sediment size/composition slicing: parameters for palaeocurrent speed and palaeoceanography: Paleoceanography, v. 10, p. 593–610, doi:10.1029/94PA03039.

McClelland, W.C., Gehrels, G.E., and Saleeby, J.B., 1992, Upper Jurassic–Lower Cretaceous basinal strata along the Cordilleran margin: implications for the accretionary history of the Alexander–Wrangellia–Peninsular Terrane: Tectonics, v. 11, p. 823–835, doi:10.1029/92TC00241.

Moffit, F.H., 1930, Notes on the geology of the upper Nizina River: U.S. Geological Survey, Bulletin 813-D, p. 143–163.

Moffit, F.H., 1938, Geology of the Chitina Valley and adjacent area, Alaska: U.S. Geological Survey, Bulletin 894, 137 p., doi:10.3133/b894.

Moffit, F.H., and Capps, S.R., 1911, Geology and mineral resources of the Nizina district, Alaska: U.S. Geological Survey, Bulletin 448, 111 p., doi:10.3133/b448.

Nelson, J.L., Colpron, M., and Israel, S., 2013, The cordillera of British Columbia, Yukon, and Alaska: tectonics and metallogeny, *in* Colpron, M., Bissig, T., Rusk, B.G., and Thompson, J.F.H., eds., Tectonics, Metallogeny, and Discovery: The North American Cordillera and Similar Accretionary Settings: Society of Economic Geologists, Special Publications, v. 17, p. 53–109, doi:10.5382/SP.17.03.

Nokleberg, W.J., Parfenov, L.M., Monger, J.W.H., Norton, I.O., Khanchuk, A.I., Stone, D.B., Scotese, C.R., Scholl, D.W., and Fujita, K., 2000, Phanerozoic Tectonic Evolution of the Circum-North Pacific: U.S. Geological Survey, Professional Paper 1626, 122 p., https://pubs.usgs.gov/pp/2000/1626/.

Omaña, L., Torres, J.R., López Doncel, R., Alencáster, G., and López Caballero, I., 2014, A pithonellid bloom in the Cenomanian–Turonian boundary interval from Cerritos in the western Valles–San Luis Potosí platform, Mexico: paleoenvironmental significance: Revista Mexicana de Ciencias Geológicas, v. 31, p. 28–44.

Peters, S.E., and Foote, M., 2002, Determinants of extinction in the fossil record: Nature, v. 416, p. 420–424, doi:10.1038/416420a.

Peybernes, C., Peyrotty, G., Chablais, J., Onoue, T., Yamashita, D., and Martini, R., 2020, Birth and death of seamounts in the Panthalassa Ocean: Late Triassic to Early Jurassic sedimentary record at Mount Sambosan, Shikoku, Southwest Japan: Global and Planetary Change, v. 192, no. 103250, doi:10.1016/j.gloplacha.2020.103250.

Plafker, G., and Berg, H.C., 1994, Overview of the geology and tectonic evolution of Alaska, *in* Plafker, G., and Berg, H.C., eds., The Geology of Alaska: Geological Society of America, The Geology of North America v. G-1, p. 989–1021, doi:10.1130/DNAG-GNA-G1.989.

Plafker, G., Nokleberg, W.J., and Lull, J.S., 1989, Bedrock geology and tectonic evolution of the Wrangellia, Peninsular, and Chugach terranes along the Trans-Alaska Crustal Transect in the Chugach Mountains and Southern Copper River Basin, Alaska: Journal of Geophysical Research: Solid Earth, v. 94, p. 4255–4295, doi:10.1029/JB094iB04p04255.

Puga-Bernabéu, Á., Martín, J.M., Braga, J.C., and Sánchez-Almazo, I.M., 2010, Downslope-migrating sandwaves and platform-margin clinoforms in a current-dominated, distally steepened temperate-carbonate ramp (Guadix Basin, Southern Spain): Sedimentology, v. 57, p. 293–311, doi:10.1111/j.1365-3091.2009.01079.x.

Puga-Bernabéu, Á., Martín, J.M., Braga, J.C., and Aguirre, J., 2014, Offshore remobilization processes and deposits in low-energy temperate-water carbonate-ramp systems: examples from the Neogene basins of the Betic Cordillera (SE Spain): Sedimentary Geology, v. 304, p. 11–27, doi:10.1016/j.sedgeo.2014.02.001.

Reading, H.G., and Richards, M., 1994, Turbidite systems in deep-water basin margins classified by grain size and feeder system: American Association of Petroleum Geologists, Bulletin, v. 78, p. 792–822, doi:10.1306/A25FE3BF-171B-11D7-8645000102C1865D.

Rebesco, M., Hernández-Molina, F.J., Van Rooij, D., and Wåhlin, A., 2014, Contourites and associated sediments controlled by deep-water circulation processes: state-of-the-art and future considerations: Marine Geology, v. 352, p. 111–154, doi:10.1016/j.margeo.2014.03.011.

Reolid, J., Betzler, C., and Lüdmann, T., 2019, Facies and sedimentology of a carbonate delta drift (Miocene, Maldives): Sedimentology, v. 66, p. 1243–1265, doi:10.1111/sed.12575.

Ritterbush, K.A., 2019, Sponge meadows and glass ramps: state shifts and regime change: Palaeogeography, Palaeoclimatology, Palaeoecology, v. 513, p. 116–131, doi:10.1016/j.palaeo.2018.08.009.

Ritterbush, K.A., Bottjer, D.J., Corsetti, F.A., and Rosas, S., 2014, New evidence on the role of siliceous sponges in ecology and sedimentary facies development in eastern Panthalassa following the Triassic–Jurassic mass extinction: Palaios, v. 29, p. 652–668, doi:10.2110/palo.2013.121.

Ritterbush, K.A., Rosas, S., Corsetti, F.A., Bottjer, D.J., and West, A.J., 2015, Andean sponges reveal long-term benthic ecosystem shifts following the end-Triassic mass extinction: Palaeogeography, Palaeoclimatology, Palaeoecology, v. 420, p. 193–209, doi:10.1016/j.palaeo.2014.12.002.

Ritterbush, K.A., Ibarra, Y., and Tackett, L.S., 2016, Post-extinction biofacies of the first carbonate ramp of the Early Jurassic (Sinemurian) in NE Panthalassa (New York Canyon, Nevada, USA): Palaios, v. 31, p. 141–160, doi:10.2110/palo.2015.021.

Rodríguez-Tovar, F.J., Nagy, J., and Reolid, M., 2014, Palaeoenvironment of Eocene prodelta in Spitsbergen recorded by the trace fossil *Phycosiphon incertum*: Polar Research, v. 33, no. 23786, doi:10.3402/polar.v33.23786.

Rodríguez-Tovar, F.J., Hernández-Molina, F.J., Hüneke, H., Llave, E., and Stow, D., 2019, Contourite facies model: improving contourite characterization based on the ichnological analysis: Sedimentary Geology, v. 384, p. 60–69, doi:10.1016/j.sedgeo.2019.03.010.

Rohn, O., 1900, A reconnaissance of the Chitina River and the Skolai Mountains, Alaska: U.S. Geological Survey, Annual Report 21, p. 393–440, doi: 10.3133/ar21_2.

Schäfer, P., and Grant-Mackie, J.A., 1998, Revised systematics and palaeobiogeography of some Late Triassic colonial invertebrates from the Pacific region: Alcheringa: An Australasian Journal of Palaeontology, v. 22, p. 87–122, doi:10.1080/03115519808619194.

Schieber, J., 2007, Microbial mats on muddy substrates: examples of possible sedimentary features and underlying processes, *in* Schieber, J., Bose, P., Eriksson, P.G., Banerjee, S., Sarkar, S., Altermann, W., and Catuneanu, O., eds., Atlas of Microbial Mat Features Preserved within the Clastic Rock Record: Amsterdam, Elsevier, Atlases in Geoscience, v. 2, p. 117–133, doi:10.1016/S1574-1966(07)02005-6.

Schieber, J., 2016, Experimental testing of the transport-durability of shale lithics and its implications for interpreting the rock record: Sedimentary Geology, v. 331, p. 162–169, doi:10.1016/j.sedgeo.2015.11.006.

Schieber, J., and Southard, J.B., 2009, Bedload transport of mud by floccule ripples: direct observation of ripple migration processes and their implications: Geology, v. 37, p. 483–486, doi:10.1130/G25319A.1.

Schieber, J., Southard, J., and Thaisen, K., 2007, Accretion of mudstone beds from migrating floccule ripples: Science, v. 318, p. 1760–1763, doi:10.1126/science.1147001.

Schieber, J., Southard, J.B., Kissling, P., Rossman, B., and Ginsburg, R., 2013, Experimental deposition of carbonate mud from moving suspensions: importance of flocculation and implications for modern and ancient carbonate mud deposition: Journal of Sedimentary Research, v. 83, p. 1026–1032, doi:10.2110/jsr.2013.77.

Schoene, B., Guex, J., Bartolini, A., Schaltegger, U., and Blackburn, T.J., 2010, Correlating the end-Triassic mass extinction and flood basalt volcanism at the 100 ka level: Geology, v. 38, p. 387–390, doi:10.1130/G30683.1.

Schrader, F.C., and Spencer, A.C., 1901, The geology and mineral resources of a portion of the Copper River District, Alaska: U.S. Geological Survey, 94 p.

Shanmugam, G., 2018, The hyperpycnite problem: Journal of Palaeogeography, v. 7, doi:10.1186/s42501-018-0001-7.

Shellnutt, J.G., Dostal, J., and Lee, T.-Y., 2021, Linking the Wrangellia flood basalts to the Galápagos hotspot: Scientific Reports, v. 11, no. 8579, doi:10.1038/s41598-021-88098-7.

Sperazza, M., Moore, J.N., and Hendrix, M.S., 2004, High-resolution particle size analysis of naturally occurring very fine-grained sediment through laser diffractometry: Journal of Sedimentary Research, v. 74, p. 736–743, doi:10.1306/031104740736.

Stow, D.A.V., and Faugères, J.-C., 2008, Contourite facies and the facies model, *in* Rebesco, M., and Camerlenghi, A., eds., Contourites: Amsterdam, Elsevier, Developments in Sedimentology, v. 60, p. 223–256, doi:10.1016/S0070-4571(08)10013-9.

Stow, D., and Smillie, Z., 2020, Distinguishing between deep-water sediment facies: turbidites, contourites and hemipelagites: Geosciences, v. 10, doi:10.3390/geosciences10020068.

Surlyk, F., 1987, Slope and deep shelf gully sandstones, Upper Jurassic, East Greenland: American Association of Petroleum Geologists, Bulletin, v. 71, p. 464–475, doi:10.1306/94886ECF-1704-11D7-8645000102C1865D.

Tew, B.H., 2000, Depositional setting of the Arcola Limestone Member (Campanian) of the Mooreville Chalk, eastern Gulf coastal plain: Gulf Coast Association of Geological Societies, Transactions, v. 50, p. 157–166.

Trop, J.M., and Ridgway, K.D., 2007, Mesozoic and Cenozoic tectonic growth of southern Alaska: a sedimentary basin perspective, *in* Ridgway, K.D., Trop, J.M., Glen, J.M.G., and O'Neill, J.M., eds., Tectonic Growth of a Collisional Continental Margin: Crustal Evolution of Southern Alaska: Geological Society of America, Special Papers, v. 431, p. 55–94, doi:10.1130/2007.2431(04).

Trop, J.M., Ridgway, K.D., Manuszak, J.D., and Layer, P., 2002, Mesozoic sedimentary-basin development on the allochthonous Wrangellia composite terrane, Wrangell Mountains basin, Alaska: a long-term record of terrane migration and arc construction: Geological Society of America, Bulletin, v. 114, p. 693–717, doi:10.1130/0016-7606(2002)114<0693:MSBDOT>2.0.CO;2.

Ward, P.D., Haggart, J.W., Carter, E.S., Wilbur, D., Tipper, H.W., and Evans, T., 2001, Sudden productivity collapse associated with the Triassic–Jurassic boundary mass extinction: Science, v. 292, p. 1148–1151, doi:10.1126/science.1058574.

Wignall, P.B., Zonneveld, J.-P., Newton, R.J., Amor, K., Sephton, M.A., and Hartley, S., 2007, The end Triassic mass extinction record of Williston Lake, British Columbia: Palaeogeography, Palaeoclimatology, Palaeoecology, v. 253, p. 385–406, doi:10.1016/j.palaeo.2007.06.020.

Wilkinson, I.P., 2011, Pithonellid blooms in the Chalk of the Isle of Wight and their biostratigraphical potential: Geologists' Association, Proceedings, v. 122, p. 862–867, doi:10.1016/j.pgeola.2011.09.001.

Winkler, G.R., and MacKevett, E.M., 1981, Geologic map of the McCarthy C-7 quadrangle, Alaska: U.S. Geological Survey, Geologic Quadrangle 1533, doi:10.3133/gq1533.

Witmer, J.W., 2007, Sedimentology and stratigraphy of the Upper Triassic–Lower Jurassic McCarthy Formation, Wrangell–St. Elias Mountains, south-central Alaska [BA Thesis]: Bucknell University, 100 p.

Yawar, Z., and Schieber, J., 2017, On the origin of silt laminae in laminated shales: Sedimentary Geology, v. 360, p. 22–34, doi:10.1016/j.sedgeo.2017.09.001.

Received 14 January 2022; accepted 12 July 2022.